Postprint of: Srokosz P., Bujko M., Bocheńska M., Ossowski R., Optical flow method for measuring deformation of soil specimen subjected to torsional shearing, MEASUREMENT, Vol. 174 (2021), 109064, DOI: 10.1016/j.measurement.2021.109064

Optical Flow Method for Measuring Deformation of Soil Sample Subjected to Torsional Shearing

Piotr E. Srokosz [1], Marcin Bujko [2], Marta Bocheńska [3,*] and Rafał Ossowski [4]

[1] University of Warmia and Mazury in Olsztyn; psrok@uwm.edu.pl
[2] University of Warmia and Mazury in Olsztyn; marcin.bujko@uwm.edu.pl
[3] University of Warmia and Mazury in Olsztyn; marta.baginska@uwm.edu.pl
[4] Gdansk University of Technology, rafal.ossowski@pg.edu.pl
* Corresponding author: marta.baginska@uwm.edu.pl

Abstract: In this study optical flow method is used for soil deformation measurement in laboratory tests. The main objective was to observe how the deformation distributes along the whole height of cylindrical soil sample subjected to torsional shearing (TS test). The experiments were conducted on dry non-cohesive soil samples under two different values of isotropic pressure. Samples were loaded with low-amplitude cyclic torque to analyze the deformation within the small strain range (0.001–0.01%). Optical flow method variant developed by Ce Liu (2009) was used for motion estimation from time-ordered series of images. This algorithm uses scale-invariant feature transform (SIFT) for image feature extraction and coarse-to-fine matching scheme for faster calculations. The results show that while the displacement values change approximately monotonically along sample's height, displacement field is very different for samples under different isotropic pressure. Moreover, the deviations from assumed linearity distribute differently during different stages of the same TS test.

Keywords: granular materials; soil; small displacement measurement; torsional shear; optical flow.

1. Introduction

Soil as a natural granular material displays complex mechanical behavior. It can react to a loading differently depending on many factors like grains sizes and shapes, density or moisture content. Despite soil's granular composition it is not uncommon that for structural design purposes it is considered to behave like a continuous material [2-4]. For simplification many models assume that some initial part of soil deformation path is purely elastic [5-9]. As most of the soil-structure interactions are within the small strain range (0.001 – 0.01%) [10,11] this simplification is very useful and it can even be a satisfactory approximation for simple and typical engineering problems. However, research shows that even the initial deformation part in soil can be more complex than that [12-15] and the soil response to stress in small strain range is not yet properly described.

To learn more about the nature of the soil mechanical response research needs to be oriented on very precise laboratory testing and observation of processes taking place in sample during the test. Yet devices for soil mechanical laboratory testing usually allow to measure only the resultant value of e.g. sample deformation. And those resultant values are often a basis for further soil parameter evaluation (like soil stiffness parameters). As far as that approach is easy to use and accessible even for non-experts, the tests do not provide us with any information about material mechanical behavior inside the sample. It is a known fact that different stress distributions can give the same resultant value measured near the boundary [16] and deformation at one point of the material sample does not indicate the deformation distribution within the whole sample. To take a measurement inside a soil sample sensors can be attached to the specimen locally inside the laboratory testing device. However, in order to learn more about the distribution of measured value one should rather use methods like X-ray computed tomography, magnetic resonance imaging (which in most cases is not economically justified) or various optical methods [17-20].

Due to the extreme importance of observation of deformations of soils tested in geotechnical laboratories, research in this field is carried out using contact and non-contact measurement

techniques. Among them there are techniques for investigating soil displacement patterns [21], wireless chemiluminescence-based sensors [22] fiber Bragg grating sensors [23], particle image velocimetry (PIV) and photogrammetry [24]. This article presents the results of the research on the applications of optical flow for measuring small strains in non-cohesive granular material subjected to torsion.

The of optical flow is a visual experience caused by the relative motion of the observer and objects in the environment. The phenomenon is most often defined as "the distribution of apparent velocities of movement of brightness pattern in an image" [25]. The optical flow concept came from the studies on animal's visual perception by American psychologist James J. Gibson in the 1950s [26]. The apparent motion of objects in the animal's field of view provides information about the spatial arrangement of the objects in space and the rate of change of this arrangement [25].

The research on the optical flow applications focuses strongly on motion estimation and video compression aspects. It is widely used in robotics for object detection and tracking or movement detection [27]. As the optical flow concept is a major aspect of a human (animal) vision, the technique is also adopted for development of machine vision [28]. The optical flow-based techniques are intensively developed and used for a wide spectrum of different purposes like fault detection in production processes [29], intelligent vehicle navigation [30], micro air vehicles control [31], structural displacement monitoring [32] and many more (see [33-35]).

In this study a method based on the optical flow is used for measuring soil deformation during torsional shearing (TS) test. Torsional shearing of soil cylindrical samples is a well-known soil testing method commonly used in geotechnical engineering from the 1930s. Initially tests based on torsional shearing were performed mainly to obtain information about mechanical properties of soils and rocks subjected to cyclic loads, especially seismic loads. The resonant frequency of the sample subjected to torsional vibrations allows for estimation of shear modulus G and damping ratio D. Those parameters can be evaluated using the elastic wave propagation theory. Laboratory devices for performing such tests are called resonant columns (RC) and were invented in Japan by Ishimoto and Iida [36] and (independently) in the USA by Birch and Bancroft [37]. Since the 1960s the resonant column has been widely used in studies of dynamic behavior of soils and rocks. In the 1990s, modifications in the device control system led to the invention of torsional shear (TS) apparatus. The TS device has found wide application in soil research under low frequency cyclic load conditions [38]. Currently, geotechnical laboratories around the world are equipped with a combined version of the RC and TS devices called multifunction RC/TS apparatus. Such a device is widely used for dynamic characterization of soils, especially for damping and stiffness measurements [39-43], applying nonlinear vibration analysis [44], the study of special granular materials (as micaceous sands [45]) and studies including hardware modifications (i.e. for the large strains [46] or permanent deformations in small strain range [47]). The originally modified construction of RC/TS apparatus working in TS mode is used in the research presented in this paper.

This paper present the results of soil displacements measurement with optical flow method. Dry non-cohesive soil cylindrical samples were subjected to low-amplitude cyclic torque, so that small strains could be analyzed. The main focus of the conducted experiments was to observe the displacements distribution along the whole sample's height and verify the linearity assumption.

2. Materials and Methods

2.1. Torsional Shearing device

The TS device used in this study is produced by Wykeham Farrance (model WF8500). Figure 1 presents the components of the device.

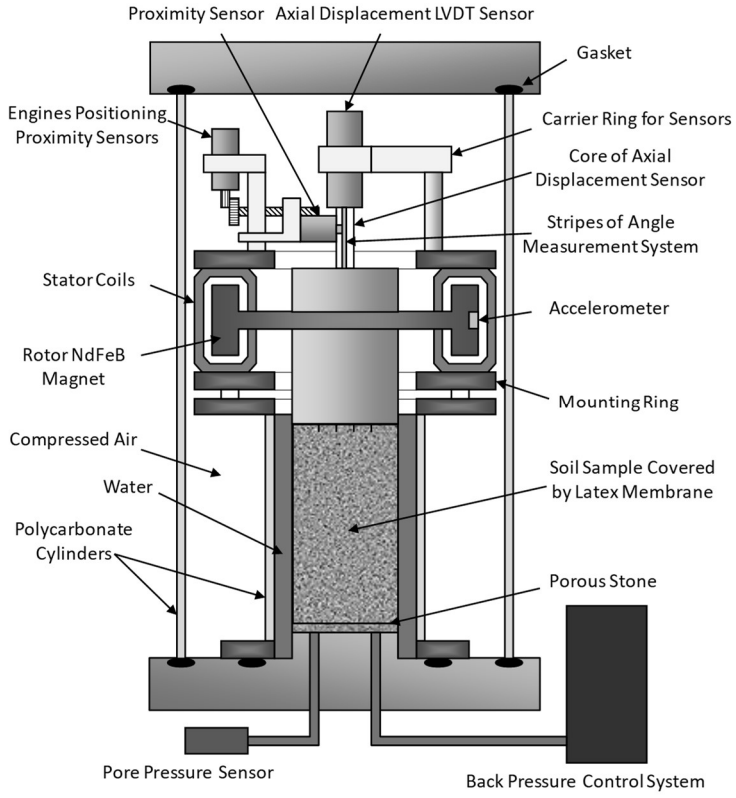

Figure 1. Components of RC/TS apparatus [48].

In TS mode a cylindrical soil sample is subjected to torque T which changes harmonically. It results in a sample twist measured by proximity transducers (Figure 2). The load frequency is below 1 Hz (typically 0.01 Hz, in modified version of the motor driver/controller even 10^{-5} Hz including different torque excitations signals like sinusoidal, trapezoidal, triangular-saw etc.).

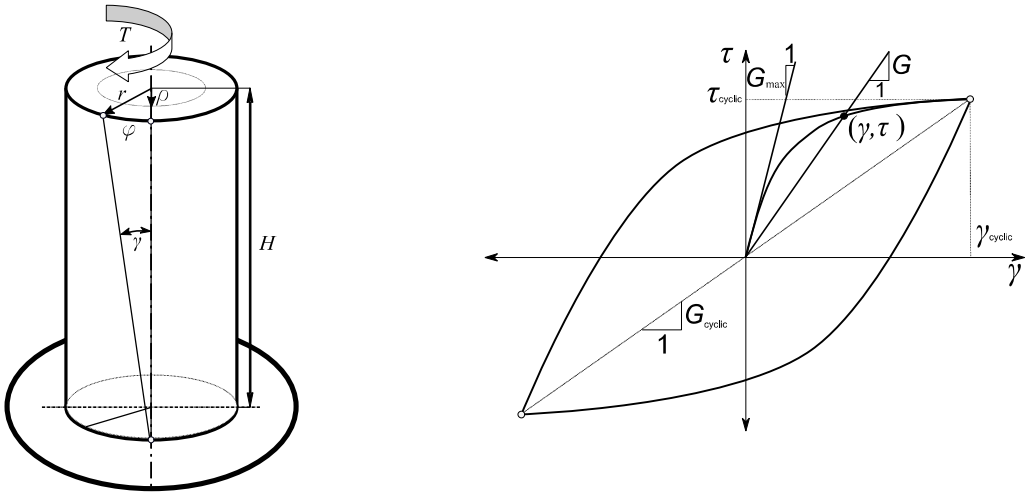

(**a**) (**b**)

Figure 2. (**a**) Torsional shearing of cylindrical soil sample (r - sample radius, ρ - sample reduced radius, H - sample height, φ - twist angle, γ - shear strain, T - torque); (**b**) Theoretical hysteresis loop of shear stress-strain relationship in cyclic shearing test (τ - shear stress, G - Kirchhoff's modulus) [49].

The measured torque and twist angle allow calculation of tangential stress and shear strain which are then used for Kirchhoff's modulus G estimation. Precise control of small torque amplitudes allows studying of soil behavior in small strain range (0.001 – 0.01%) which is typical for commonly encountered soil-structure interactions [10,11].

Figure 2(b) shows an idealized stress–strain relation obtained for cyclic load (symmetric periodic waves) of a predetermined amplitude. The obtained stress–strain relations form a hysteresis loop. The soil's mechanical response in form of the hysteresis loop indicates that the material accumulates elastic energy of reversible deformations but loses some energy due to damping. The lost part of energy is equal to the work done by applied external force (the torque). What's important is that the results interpretation is based on the assumption that the soil reacts like a continuous viscoelastic material. During the test the shearing angle is measured only in the sample cross-section near its upper end. The deformation is assumed to be linearly distributed along the sample's height. However, there is no evidence that the sample always deforms proportionally over its entire height (see Figure 3). In this study a method of surface displacements observation using optical flow is proposed to verify this assumption.

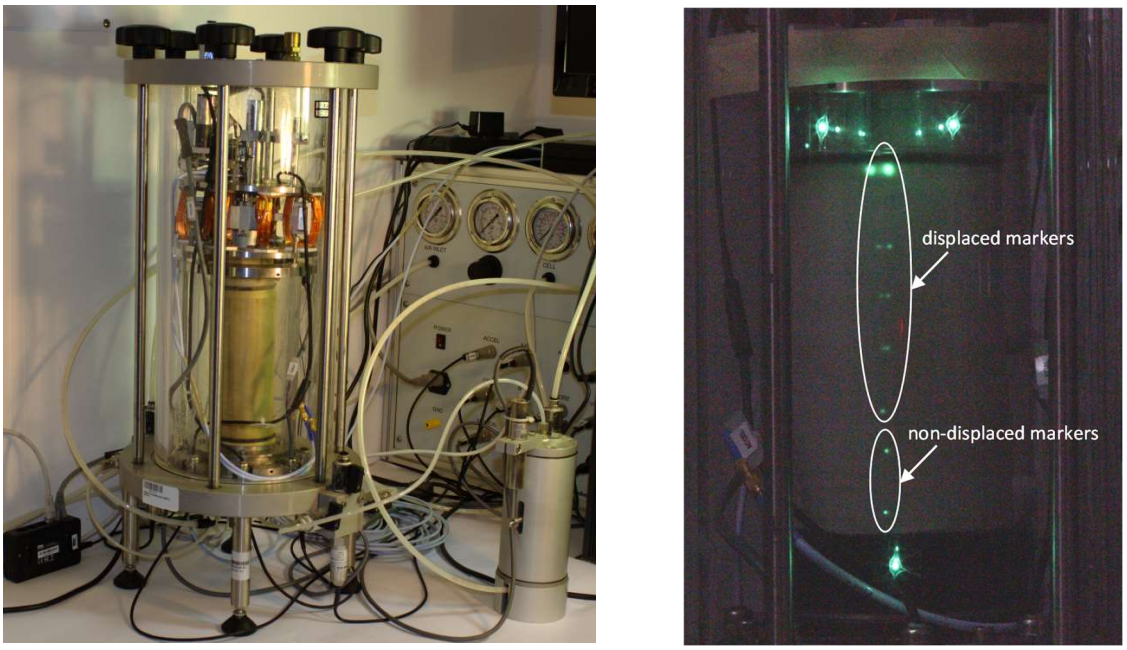

(**a**) (**b**)

Figure 3. (**a**) The TS device; (**b**) Result of optical measurement of phosphorescent markers during TS test with visible non-displaced points [50].

2.2. *Material used in tests*

A few types of granular, non-cohesive materials were selected for the study, which were prepared according to [51] (the specimen was prepared from pre-formed non-cohesive soil fractions). However, for a greater clarity the results for specimens made of one type of soil are presented (results for the other types do not differ much in terms of quality). The properties of soil selected for further analyses are summarized in Table 1. The shape of grains is shown in Figure 4. Figure 5 presents grain size distribution of tested material.

Table 1. Parameters of tested soil

Soil type	G_s [-]	d_{50} [mm]	d_{60} [mm]	d_{10} [mm]	d_{90} [mm]	C_U [-]	e [-]	ρ [g/cm^3]
sand	2.65	0.33	0.35	0.22	0.55	1.6	0.50	1.76

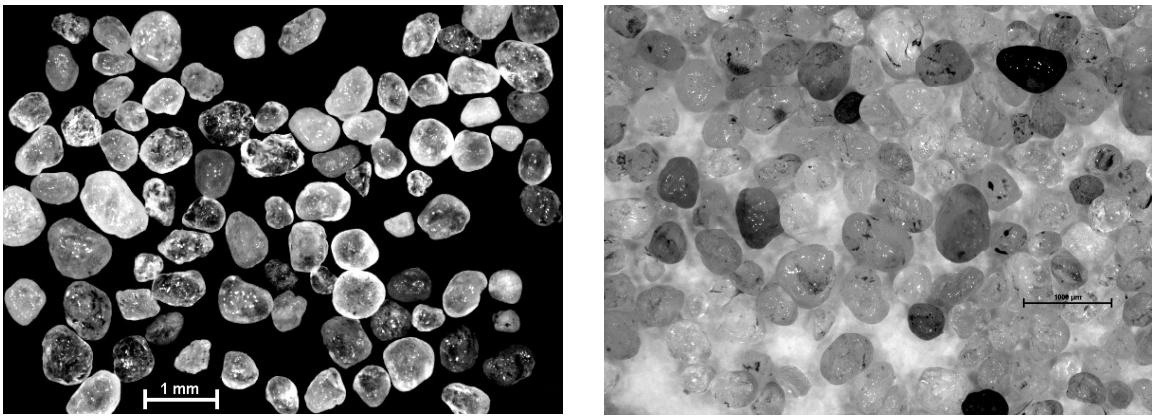

(**a**) (**b**)

Figure 4. Tested material. Grains in magnification (**a**) on a black background; (**b**) on a white background.

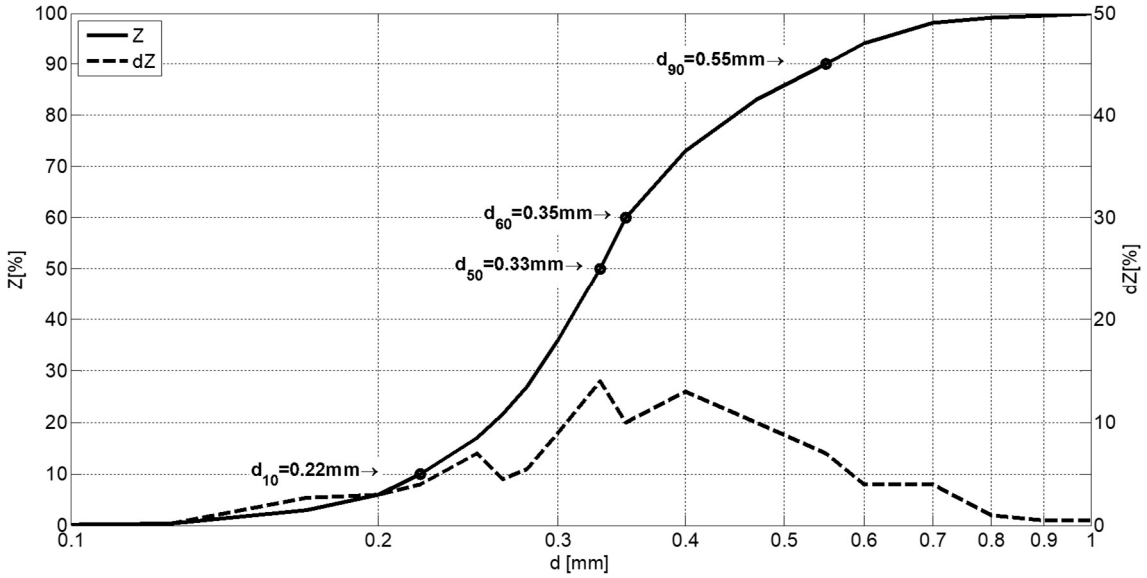

Figure 5. Grain size distribution in the tested material (d - equivalent particle diameter, Z - cumulative less than indicated size, dZ - volume share per particle size interval).

2.3. Optical flow estimation

In this section we describe two approaches of determining the displacement field using recognition of spatiotemporal patterns of image intensity, brightness [52] and color [27, 53] flow techniques.

2.3.1. Brightness optical flow

The optical flow methods use time-ordered image sequences to estimate the motion (velocities or discrete displacements) of objects in the image series. The methods use partial derivatives with respect to the spatial and temporal coordinates to calculate objects' current velocity.

To describe the motion between two image frames taken at points t and $t + \Delta t$ in time at every position on a 3D grid the optical flow methods use Taylor series approximations of the object motion trajectory.

In camera-centered coordinates each point in a 3D space moves along a 3D path. When projected onto the image plane each point moves along a 2D path. Considering the 2D+t case, when image pixels with coordinates (x_1, x_2, t) and intensity $I(x_1, x_2, t)$ move by $\Delta x_1, \Delta x_2$ over time Δt, a new image is obtained $I(x_1 + \Delta x_1, x_2 + \Delta x_2, t + \Delta t)$. It is assumed that pixel intensities are constant between the frames (the brightness constancy constraint)

$$I(x_1, x_2, t) = I(x_1 + \Delta x_1, x_2 + \Delta x_2, t + \Delta t), \tag{1}$$

as the movement is assumed to be small. Removing higher order terms from the Taylor series

$$I(x_1 + \Delta x_1, x_2 + \Delta x_2, t + \Delta t), \\ = I(x_1, x_2, t) + \frac{\partial I}{\partial x_1}\Delta x_1 + \frac{\partial I}{\partial x_2}\Delta x_2 + \frac{\partial I}{\partial t}\Delta t + higher\ order\ terms \tag{2}$$

we get

$$\frac{\partial I}{\partial x_1}\Delta x_1 + \frac{\partial I}{\partial x_2}\Delta x_2 + \frac{\partial I}{\partial t}\Delta t = 0 \tag{3}$$

Dividing (2) by Δt we obtain the optical flow equation

$$\frac{\partial I}{\partial x_1}u_1 + \frac{\partial I}{\partial x_2}u_2 + \frac{\partial I}{\partial t} = 0, \tag{4}$$

where $u_1 = \Delta x_1/\Delta t$ and $u_2 = \Delta x_2/\Delta t$ are the components of the velocity, $\partial I/\partial x_1$, $\partial I/\partial x_2$ and $\partial I/\partial t$ are the image gradient components along the horizontal axis, the vertical axis, and time.

As there are two unknowns (u_1, u_2) and only one equation (4) the problem cannot be solved without introducing additional constraints. To address this issue the optical flow methods are using different additional equations (e.g. global smoothness constraint, known as Horn-Schunck method [25] or constant flow in a local neighborhood, known as Lucas-Kanade method [54]).

Apart from the Gradient-Based methods many methods of optical flow estimation are used to approximate motion field from time-varying image intensity including correlation, block-matching, feature tracking or energy based methods. Despite the differences between optical flow techniques, many of them generally follow three processing stages listed below [55].

1. Pre-filtering or smoothing with low-pass/band-pass filters in order to extract signal structure of interest and to enhance the signal-to-noise ratio.
2. Extraction of basic measurements such as spatiotemporal derivatives (to measure normal components of velocity) or local correlation surfaces.
3. Integration of these measurements to produce a 2D flow field which often involves assumptions about the smoothness of the underlying flow field.

A major drawback of the Gradient-Based Estimation method is its sensitivity to conditions commonly encountered in real imagery. Highly textured regions, motion boundaries and depth discontinuities might be troublesome. In practice, for the observed brightness (image intensity) of any object point to be constant over time the following conditions need to be satisfied

- surface radiance remains fixed from one frame to the next,
- non distant point source (object) ,
- light distance is constant or changing the distance has no effect,
- no object rotations,
- no secondary illumination.

In experiments performed in this study the aforementioned conditions were satisfied.

2.3.2. Color optical flow

The color optical flow was first mentioned in the work of Ohta [56] and the first proposal of methods for solving the optical flow constraint equation extended to color images can be found in [57] (see [53]).

The optical flow analysis of color images has three main advantages

- the color can as well be treated in the same way as shades of gray,
- the color components can carry additional information about the position of the analyzed points on the compared images,

- the color components can be processed independently of each other.

Considering the last aspect of possible analyzes of optical color flow the optical flow equation (4) can be applied to each color channel. That is, each component of color represented in a specific color space creates an individual differential equation analogous to (4), fulfilling the *color conservation*

$$\nabla I(\boldsymbol{x},t)_C \cdot \boldsymbol{u} + I(\boldsymbol{x},t)_C = 0, \tag{5}$$

where $\boldsymbol{x} = (x_1, x_2)$ is the displacement, $\boldsymbol{u} = (u_1, u_2)$ is the velocity and the subscript C denotes the analyzed color component in the color space. The most commonly used color spaces are RGB, HSV, YUV, HSL, CMYK, CIEXYZ, CIELab, CIELUV etc.

Andrews & Lovell [53] proposed two methods for achieving a solution of the problem reducing the number of equations by disregarding the selected color component or using optimization techniques (i.e. least squares).

2.3.3. Scale-Invariant Feature Transform method (SIFT)

Scale Invariant Feature Transform is an algorithm for local feature detection in images. The method was originally developed by David G. Lowe in 1999. It is used in computer vision for image matching and object recognition. The information about the local image features extracted by SIFT algorithm is invariant to scale, translation and rotation in the image domain [58]. SIFT can be used to measure velocities, displacements and deformations based on the analysis of local features of recorded image series. The method consists in finding similarities in the analyzed images basing on distinguished features. Those features are characteristic patterns of pixels, usually found on high contrast regions like edges and peaks.

The SIFT algorithm starts with selection of potential location for finding features. When the feature keypoints are localized the rotation invariance is achieved by assigning orientation to the keypoints. The obtained keypoints are recorded as a high dimensional feature vectors called SIFT keys. This approach transforms an image into a large collection of the SIFT keys. Each of them is invariant to image translation, scaling, 3D projection. As author highlights [58] method is also less sensitive to projective distortion and illumination change, which is a significant advantage over other similar methods.

Ce Liu in his Ph.D. thesis in 2009 [1] proposed a SIFT flow method which was formulated just like the optical flow but instead of the pixels' RGB values the SIFT descriptors were used for matching between image frames. SIFT method was used for feature extraction purposes. Every pixel was assigned the 128-D vector containing information about the pixel's nearest neighbors.

When matching two "SIFT images" (features) s_1 and s_2 the goal is to minimize an energy function E of displacement $\boldsymbol{w}(\boldsymbol{p}) = (u(\boldsymbol{p}), v(\boldsymbol{p}))$, where $\boldsymbol{p} = (x, y)$ is a pixel. The $u(\boldsymbol{p})$ and $v(\boldsymbol{p})$ values are limited to integers so the number of possible states is significantly reduced. The following form of the energy function is introduced (similar to optical flow)

$$\begin{aligned} E(w) = \sum_{\boldsymbol{p}} min\left(\left\|s_1(\boldsymbol{p}) - s_2\left(\boldsymbol{p} + \boldsymbol{w}(\boldsymbol{p})\right)\right\|_1, d_1\right) + \sum_{\boldsymbol{p}} \eta(|u(\boldsymbol{p})| + |v(\boldsymbol{p})|) \\ + \sum_{(\boldsymbol{p},\boldsymbol{q})\in\varepsilon} min(\alpha|u(\boldsymbol{p}) + u(\boldsymbol{q})|, d_2) + min(\alpha|v(\boldsymbol{p}) + v(\boldsymbol{q})|, d_2) \end{aligned} \tag{6}$$

where ε is a set of neighborhoods of $\boldsymbol{p}$ and d_1, d_2 are thresholds. The energy function consist of three components. The first term is for finding pixels with similar SIFT descriptors in the next frame. The second term ensures that pixels found are close to $\boldsymbol{p}$ (i.e. $\boldsymbol{w}(\boldsymbol{p})$ is as small as possible). And the third term constraints the set of solutions so that flow of pixels from neighborhood of $\boldsymbol{p}$ is similar to $\boldsymbol{w}(\boldsymbol{p})$ (smoothness term).

The method consists in the successive search for all possible variants of displacement of the analyzed pixel structure which can take a lot of time (more than 2h for a pair of 256×256 images with a 16GB memory usage [1]). Ce Liu has simplified the algorithm by applying coarse-to-fine matching scheme. Instead of analyzing all the possibilities of movement in detail, it is searching for larger

structures (coarse) and for similarities (fewer opportunities) first, and then for the details (fine). This approach significantly shorten the time of the necessary calculations (for the same pair of images it took about 30 s on a two quad-core 2.67 GHz CPUs and 32 GB memory [1]).

The coarse-to-fine matching not only speeds up the process but also minimize energy function better in most cases compared to the ordinary scheme [1].

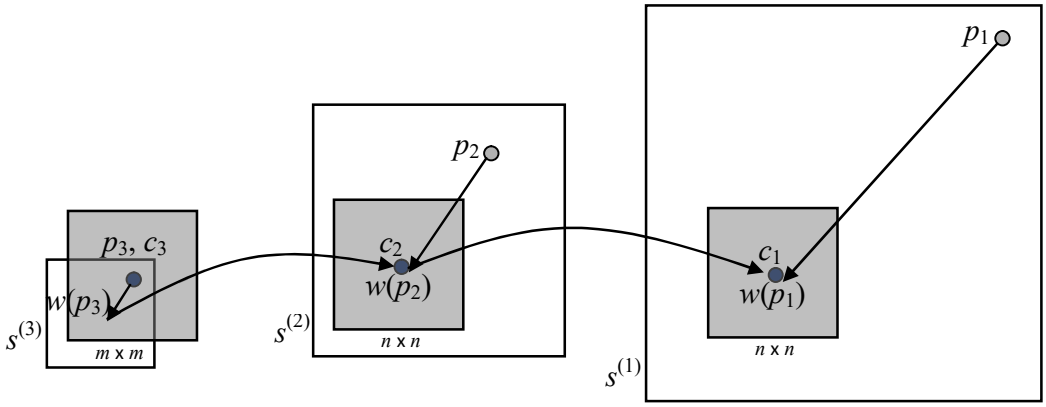

Figure 6. The coarse-to-fine SIFT flow matching scheme [1].

The idea of coarse-to-fine SIFT flow matching is illustrated in Figure 6. The searching for the best match starts at the least detailed image version $s^{(3)}$. Lowered image resolution makes the general direction of movement easier to find. Also the search window c_3 (the gray square) centered on the point p_3 is relatively large compared to the image size $m \times m$. The flow vector $w(p_3)$ is propagated to more detailed images $s^{(2)}$ then $s^{(1)}$ and it can be more precisely determined with every step. Searching the whole area of the original picture $s^{(1)}$ would be far more time-consuming. This procedure significantly lowers the level of computational complexity what results in faster calculations.

The source code of Ce Liu's SIFT flow is publicly available [1]. Since the program needs some human assistance with managing the image layers and objects properly, the graphical user interface allows the user to easily specify some of the key aspects of motion analysis. In more detail, the user can define layer configurations, objects contours, specify the depth of each object. The user needs to specify those at one or several key frames and the program automatically tracks the contours for the rest of the frames.

Author mentions that object tracking process can go wrong unless the occlusion is modeled properly. The system allows the user to change the depth of the object which is automatically interpolated with a smooth depth function. HSV color space (see Figure 7 and interesting HSV manipulations in [59]) has been applied to indicate the depth, by fixing S (saturation) and V (value) as 255, and letting H (hue) reflect the depth value. Warmer color (closer to red) indicates smaller value of depth, closer to the camera, whereas colder color (closer to blue) indicates larger value of depth, further of the camera.

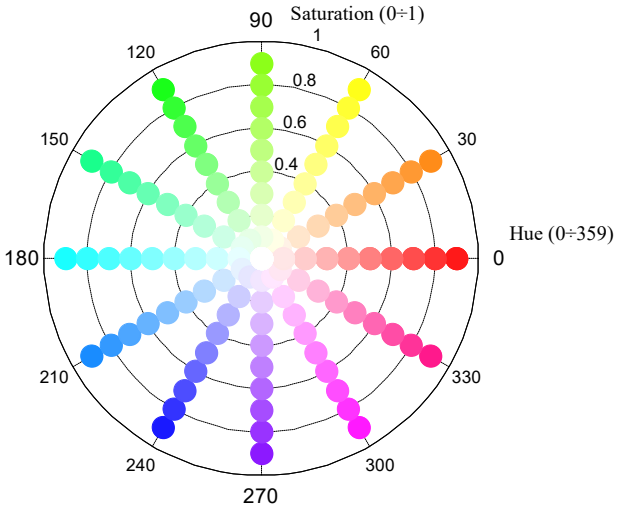

Figure 7. HSV color space used for occlusion handling (for value V=1).

2.4. Specimen preparation

A cylindrical soil specimen was formed using a template with latex membrane installed inside it. Each cylindrical specimen was compacted with a hand rammer in five layers of dry sand, taking care not to damage the texture covering the lateral outer surface of the membrane (Figure 8). Each specimen had diameter $D = 70\ mm$ and height $H = 140\ mm$.

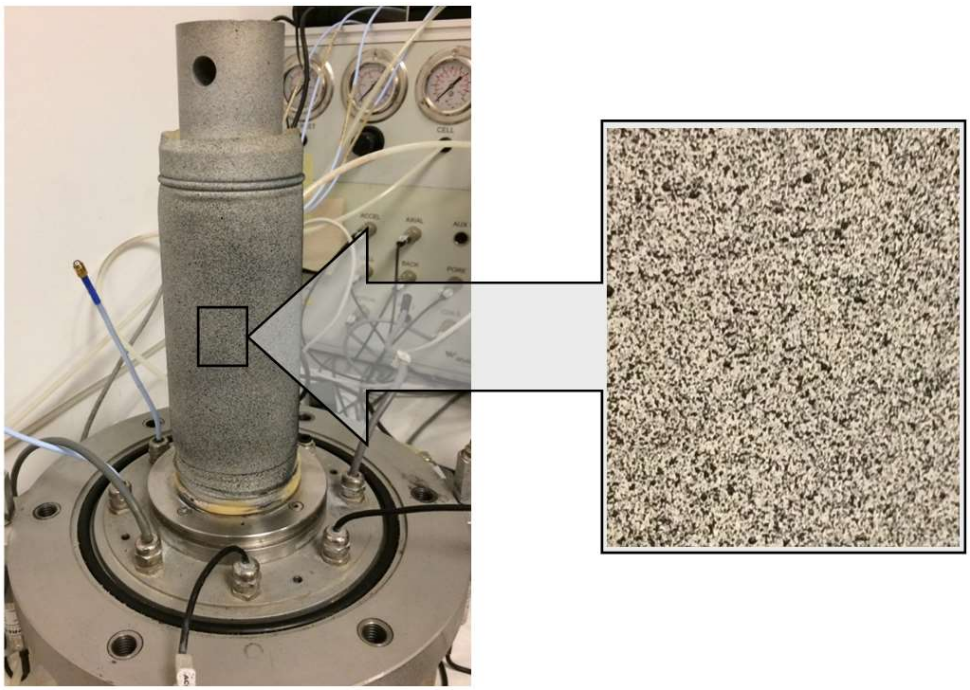

Figure 8. Soil specimen in latex membrane covered with fine pattern

Optical displacements tracking requires a pattern consisting of light and dark points on the sample surface (see Figure 8). To satisfy this requirement the texture covering the membrane was prepared by first applying a thin primer of white paint and then gently spraying black paint, trying to get the highest contrast between the neighboring points. It should be noted that the paint layers were so thin that they did not change the mechanical properties of the latex membrane. However, it was noted that despite the use of waterborne paints, long-term contact of the paint (e.g. over 2 months) led

to chemical degradation of latex. Therefore, the membranes were prepared immediately before each test.

Weight and geometrical dimensions of formed specimens were precisely controlled and meticulously recorded. Due to the large number of samples prepared this way in the last few years, the reproducible mechanical features of all the prepared samples were obtained.

After the specimen was formed inside the TS apparatus, the soil was subjected to an isotropic pressure (0.2-30 kPa) for one hour. Then, a cyclic twisting test was carried out with the test parameters shown in Table 2. 17 tests were performed in total. Two examples of tests were selected to present in detail in this paper. The first test was carried out at isotropic pressure close to zero (i.e. close to atmospheric pressure) to ensure noticeable residual deformation. The second test was performed at pressure corresponding to the natural conditions of the bed from which sand was collected. Tests were carried out with the minimum frequency and number of cycles that can be programmed on the WF8500 apparatus. However, the load amplitude was selected by trial and error method so that the displacements were in the desired strain range (0.001-0.01%) for each specimen.

Table 2. TS tests parameters

Sample	Confining pressure [kPa]	Amplitude [V]	Frequency [Hz]	Number of cycles [-]	Observation time after the test [h]
TS1458	0.2	1.0	0.01	3	4.4
TS5517	26.6	9.0	0.01	3	4.4

2.5. Experimental setup

The experimental setup consisted of a torsion shear apparatus WF8500, a 5 megapixel digital camera installed on the ARAMIS 5M (system for high-precision motion measuring) and 1000 W halogen lamp (Figures 9 and 10).

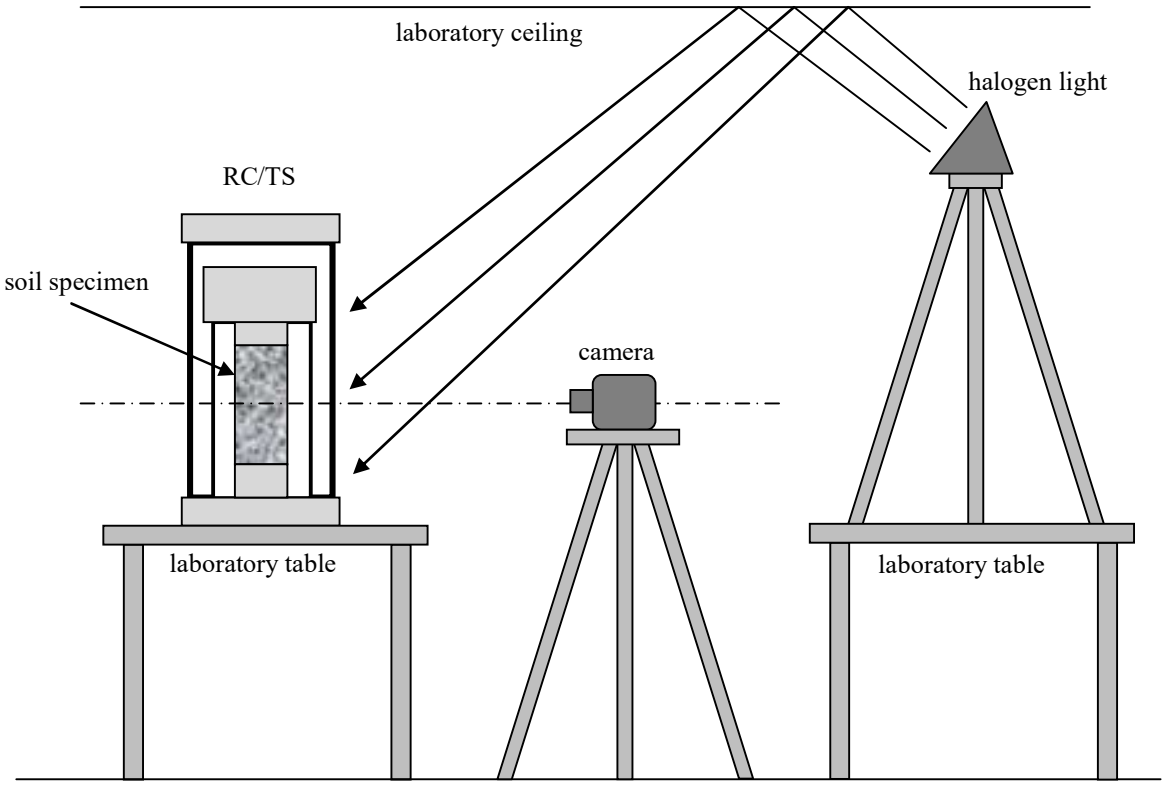

Figure 9. The experimental setup scheme

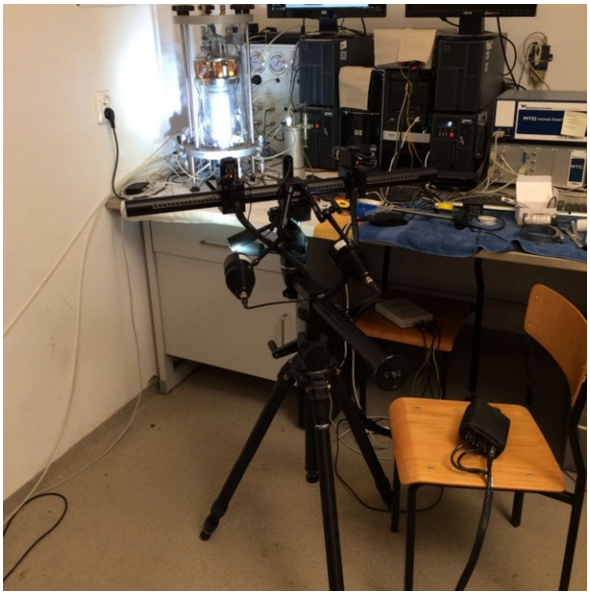

Figure 10. The experimental setup. The sample is illuminated directly to focus the camera.

Photos were taken at one second intervals. Despite all efforts, the digital image correlation built into the ARAMIS system was unusable due to interference created by two cylinders made of polycarbonate that isolated the soil sample from the environment. Another important issue was the optimal illumination of the lateral surface of the sample. The lighting had to be dispersed so that it would not cause reflections from the walls of the polycarbonate cylinders. It was found that the best way to ensure optimal conditions for taking pictures is to illuminate the specimen with light reflected from the white ceiling of the laboratory. However, to focus the camera, the sample was temporarily illuminated directly by the LED lamp (Figure 10).

2.6. Input data processing

Photos taken with the ARAMIS system camera had the resolution of 2448x2050 pixels. In the case of 256 shades of gray encoded with one byte for each image pixel, this gave a total volume of a single image frame of 5,018,400 bytes. The analysis of 500 photos taken during other study lasted over 10 hours (four threads parallel computation on Core i7 4790K @4.4GHz). However, limiting the area of recorded photos only to the sample region significantly shortened the computation time (by over 70%). The extraction of an interesting fragment of an example photo is presented in Figure 11.

Test photos present the specimen placed behind two transparent polycarbonate cylinders (Figure 13(a)). Due to those obstacles in the path of the light beam registered by the camera, image corrections related to the light refraction were necessary. A well-known Snell's Law was used for ray tracing [60]

$$\boldsymbol{t} = \frac{\eta_1}{\eta_2}\boldsymbol{i} + \left(\frac{\eta_1}{\eta_2}\cos\theta_i - \sqrt{1-\sin^2\theta_t}\right)\boldsymbol{n}, \tag{7}$$

$$\boldsymbol{t} = \frac{\eta_1}{\eta_2}[\boldsymbol{n}\times(-\boldsymbol{n}\times\boldsymbol{i})] - \boldsymbol{n}\sqrt{1-\left(\frac{\eta_1}{\eta_2}\right)^2(\boldsymbol{n}\times\boldsymbol{i})\cdot(\boldsymbol{n}\times\boldsymbol{i})}, \tag{8}$$

where: η_1 and η_2 are refractive indices of two materials (air|polycarbonate or polycarbonate|air), $\boldsymbol{i}$ and $\boldsymbol{t}$ are normalized direction vectors of the incident and transmitted rays, $\boldsymbol{n}$ is a normalized normal vector, orthogonal to the interface and pointing towards the first material (i.e. material with a refractive index η_1), θ_i and θ_t are angles of incidence and refraction, $\times$ and $\cdot$ are cross and dot products, respectively.

To determine the values of the refractive indices η for air the approximation formula available in [61] was used (the arguments of this formula are wavelength, temperature, pressure, relative humidity

and CO_2 concentration). The value of the refractive index for polycarbonate was taken from [62]. Additional image correction was also applied because of the cylindrical side surface of the sample.

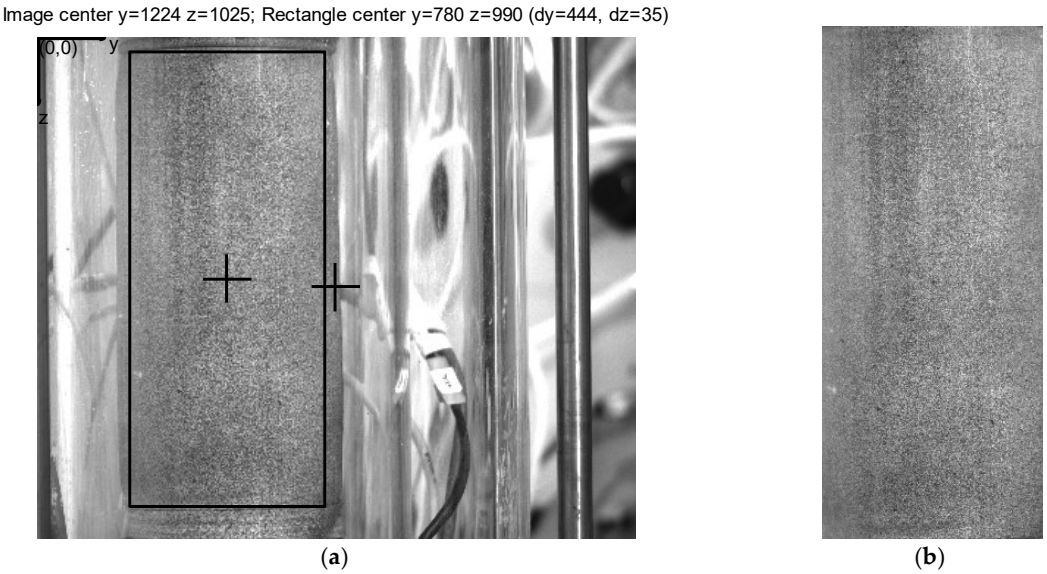

Figure 11. The area of interest extracted from the photo: (**a**) Original image; (**b**) Extracted area.

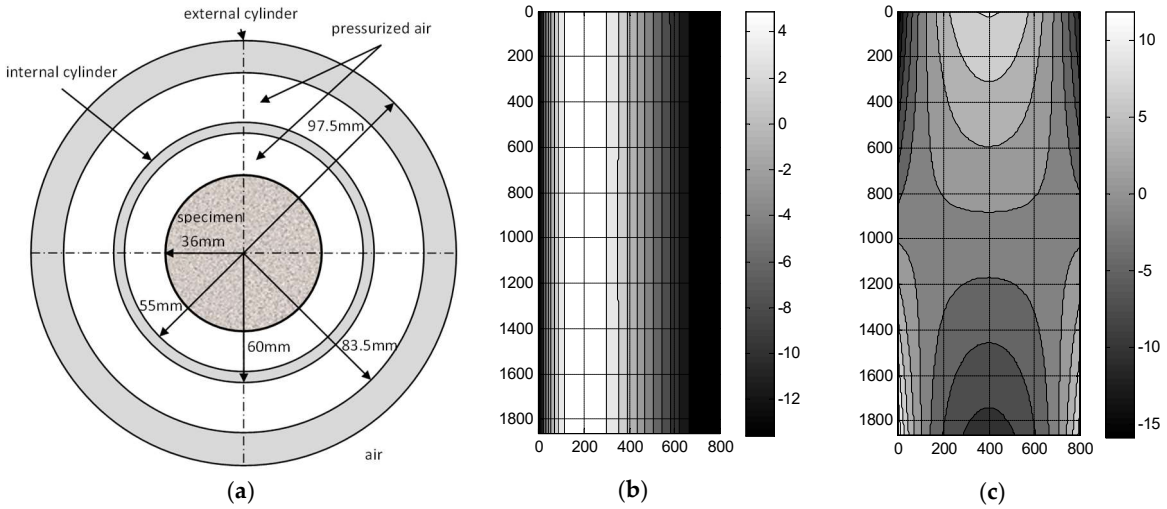

Figure 12. (**a**) Geometric data for refraction correction. Correction maps for the photo shown in Figure 11. (**b**) Width correction *dy* [mm]. (c) Height correction *dz* [mm].

Examples of the correction results are shown in Figures 12(b) and 12(c). It should be emphasized that the application of the above corrections is conditioned by the accuracy of the localization of the camera lens and the RC/TS chamber with the sample. However, the sensitivity analysis carried out showed that geometric measurements are not critical to the results of the analyzes (i.e. a few centimeter error in measuring the distance of the camera from the sample surface does not noticeably affect the results of the deformation analysis). Figure 13 shows the steps of cropped photos pre-processing.

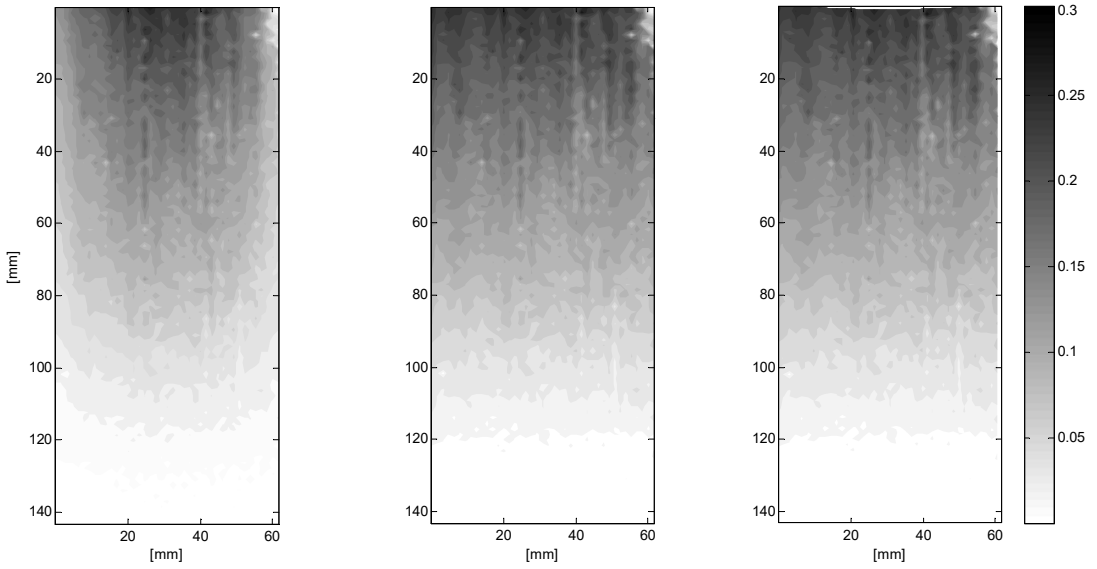

Figure 13. Stages of cropped image processing (horizontal displacements [mm] in reduced resolution (sample TS1458): grid 41x94 points). (**a**) Raw results. (**b**) Results after curvature correction. (**c**) Final results after curvature and refraction correction.

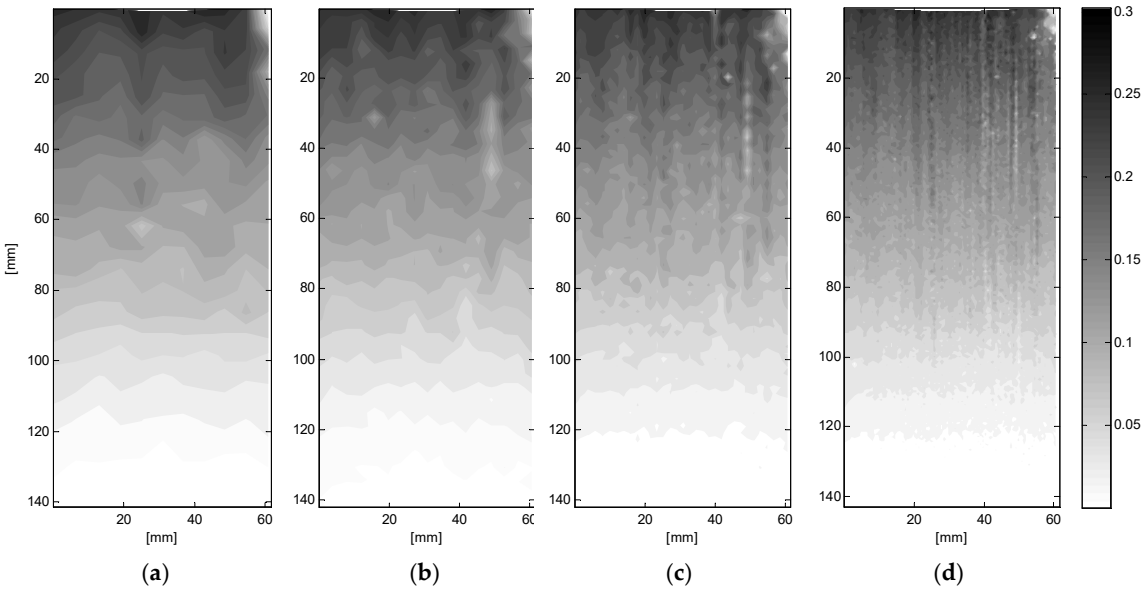

Figure 14. Horizontal displacement field [mm] in different resolutions (sample TS1458). (**a**) Grid 24x11. (**b**) Grid 38x17. (**c**) Grid 33x75. (**d**) Grid 81x187.

Another aspect of image analysis is the number of points needed for a comprehensive visualization of deformations. The cropped images contained approximately 1.5 million pixels. Although clear visualization of displacement fields does not require such high resolution (see Figure 14), the final analyzes presented in this paper were made for full image resolution.

3. Results

The optical flow code developed in the MATLAB environment by Ce Liu [1] was used in the performed analyzes. The results obtained from optical flow analysis were correlated with known displacements at two reference levels, twisting top cap (measured independently with two proximity sensors) and fixed bottom cap (no displacement). Optical flow algorithm parameters have been optimized as a result of multiple trial and error calculations and are summarized in Table 3

(with their default values suggested by Ce Liu [1]). The algorithm of the full analysis procedure is shown in Figure 15.

Table 3. The optical flow algorithm parameters (see [1]).

Values	Regularization weight	Down-sample ratio	Width of the coarsest level	Number of outer fixed point iterations	Number of inner fixed point iterations	Number of successive over-relaxation iterations
default	1	0.5	40	3	1	20
optimal	0.02	0.75	20	10	3	40

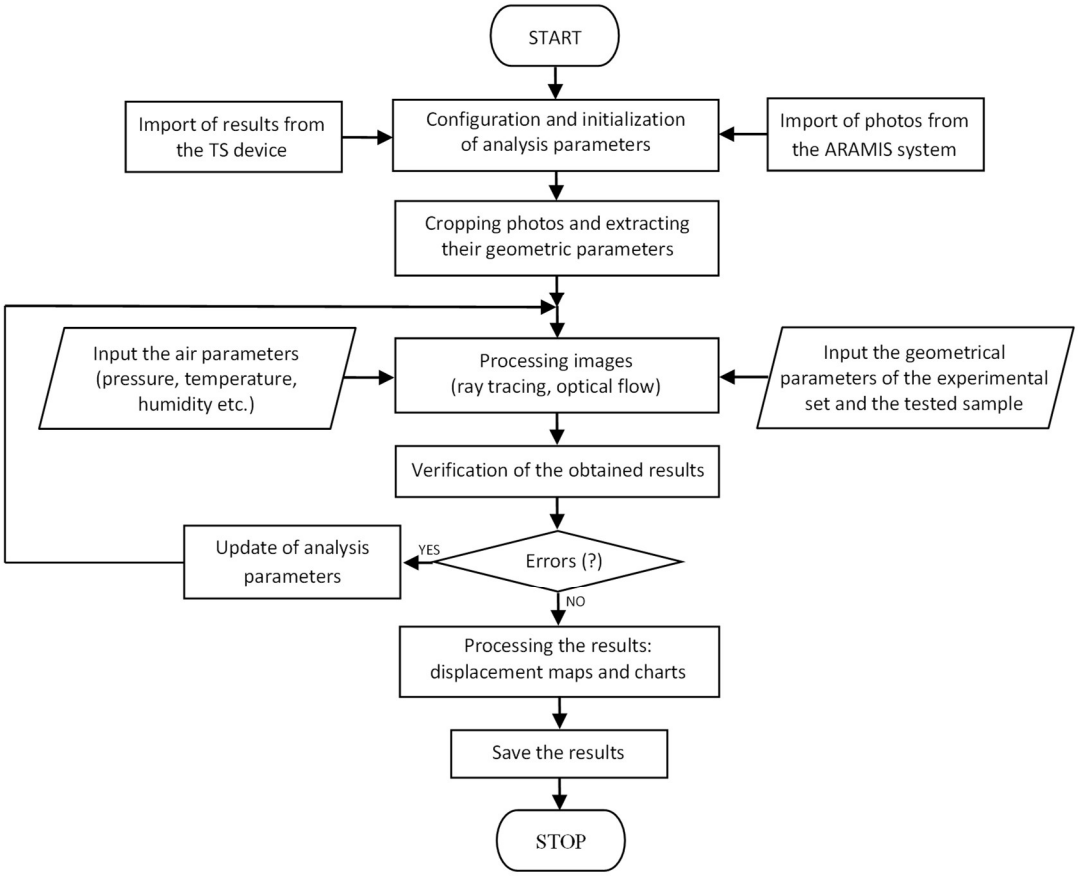

Figure 15. The analysis procedure algorithm

The results for the sample TS1458 (subjected to lower confining pressure, see Table 2) are presented on Figures 16-26 in the following manner. Figure 16 shows the torsional shear test results (typical for samples of this soil tested with similar parameters). Figures 17-26 present the
(a) horizontal,
(b) vertical
displacement fields at crucial moments of the TS test, that is the maximum and minimum twist amplitude and the residual state.

The most important goal of the experiments was to determine whether the horizontal displacements of the sample, observed on its side surface, change linearly with its height. It can be noticed, after averaging the values of horizontal displacements in the band of the assumed width (10, 50 and 200 points-pixels) along the sample axis, that this relationship is not linear (see Figures 18-20 and 22-23; vertical displacement analysis has a negligible impact on the determination of the

shear modulus G). Particular attention should be paid to the fact that deviations from the assumed linearity distribute differently on sample's height during different stages of the same TS test (compare Figures 20 and 23).

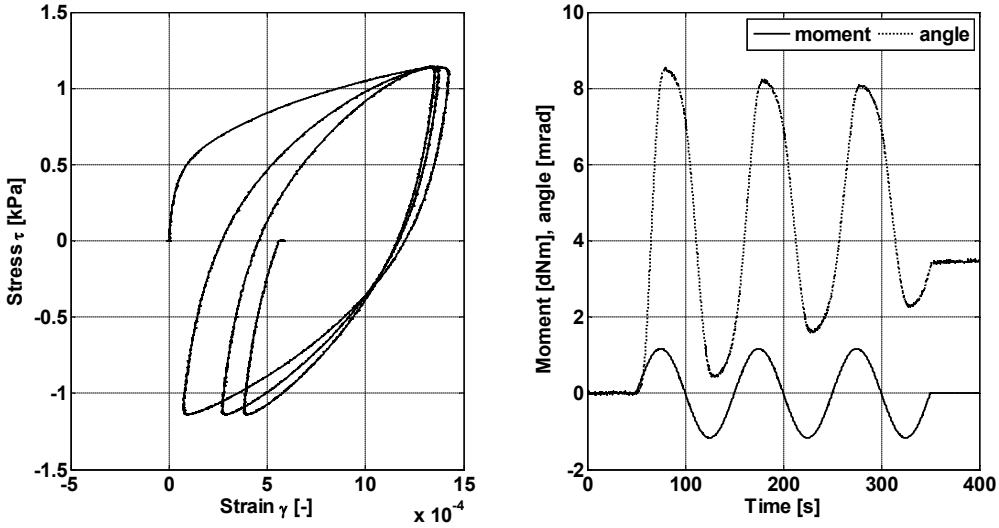

Figure 16. Typical TS test results (sample TS1458)

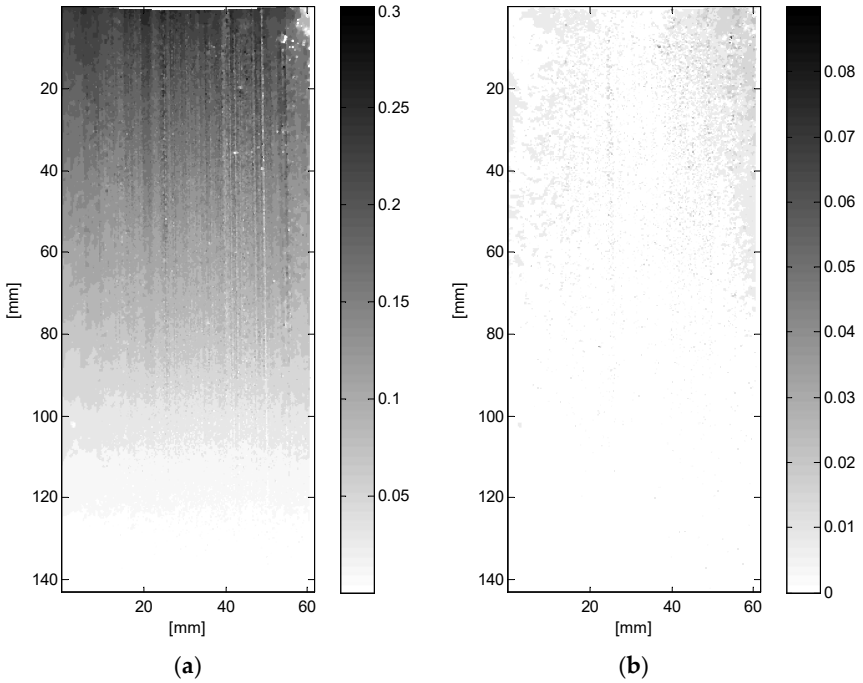

(**a**) (**b**)

Figure 17. Results of optical flow analysis in full resolution (sample TS1458, grid 801x1861 points). (**a**) Horizontal displacements [mm] at maximum twist. (**b**) Corresponding vertical displacements [mm].

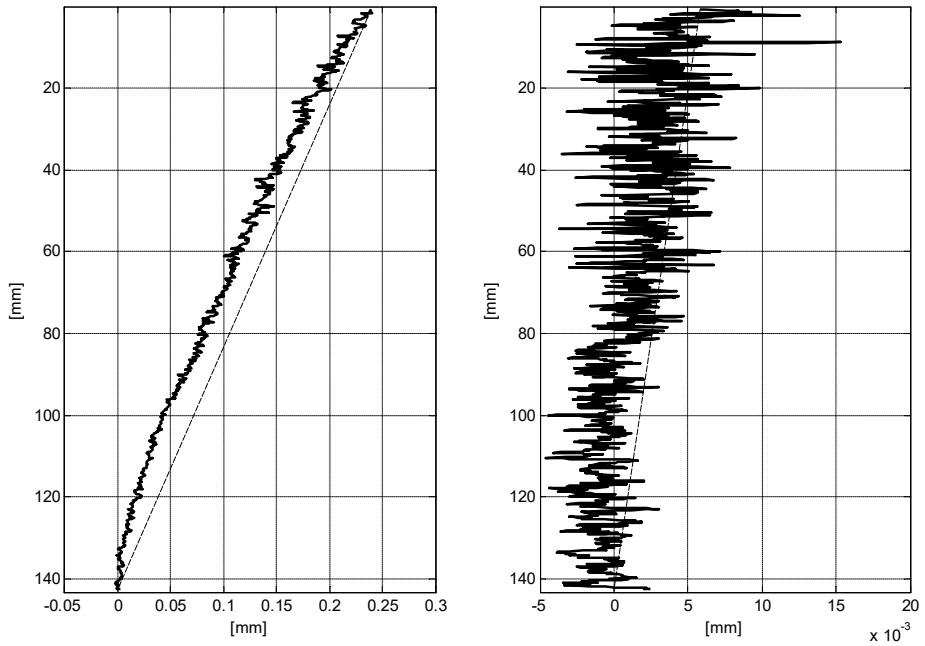

(**a**) (**b**)

Figure 18. Results of optical flow analysis (sample TS1458, averaging width: 10 pixels). (**a**) Horizontal displacements [mm] along the specimen height at maximum twist; (**b**) Corresponding vertical displacements [mm]; (dashed line is the assumed linear relationship between displacement and sample height).

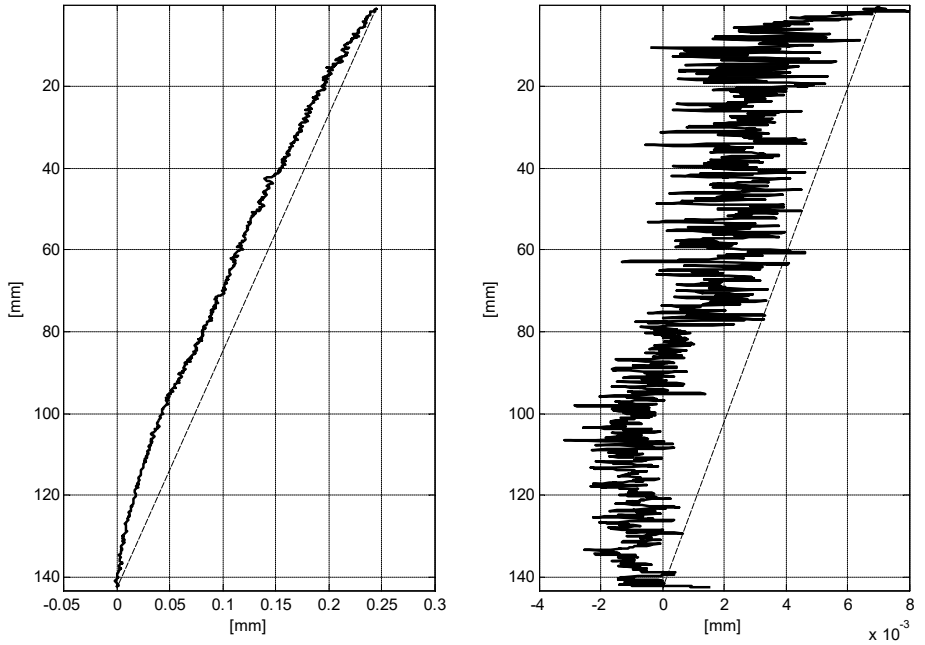

(**a**) (**b**)

Figure 19. Results of optical flow analysis (sample TS1458, averaging width: 50 pixels). (**a**) Horizontal displacements [mm] along the specimen height at maximum twist; (**b**) Corresponding vertical displacements [mm]; (dashed line is the assumed linear relationship between displacement and sample height).

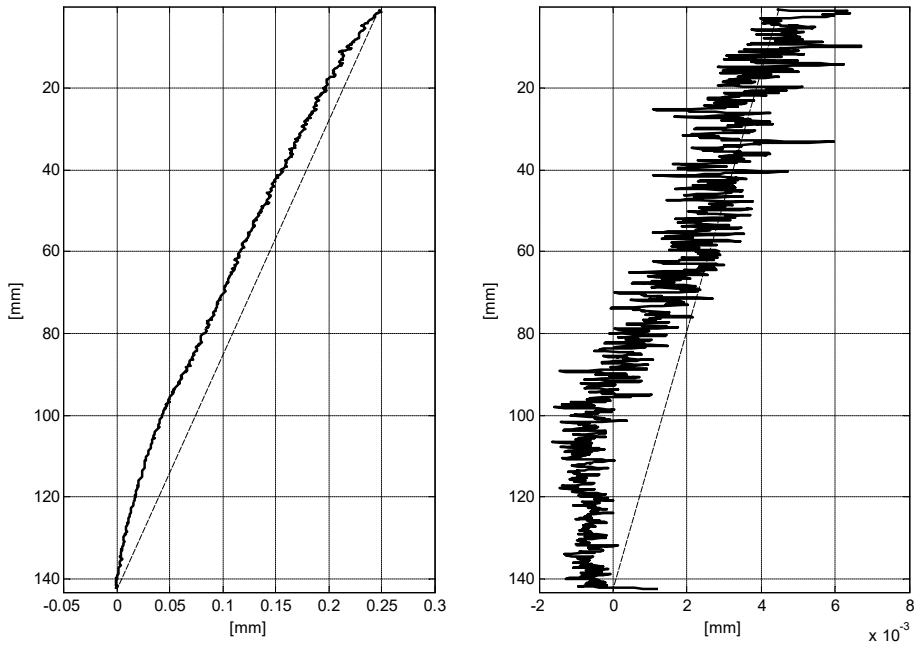

Figure 20. Results of optical flow analysis (sample TS1458, averaging width: 200 pixels). (**a**) Horizontal displacements [mm] along the specimen height at maximum twist; (**b**) Corresponding vertical displacements [mm]; (dashed line is the assumed linear relationship between displacement and sample height).

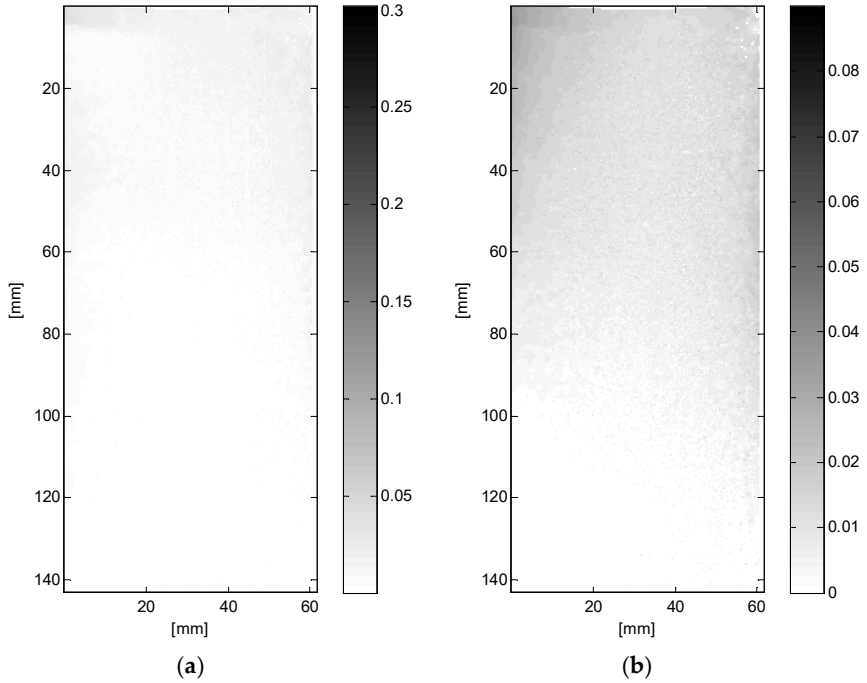

Figure 21. Results of optical flow analysis in full resolution (sample TS1458, grid 801x1861 points). (**a**) Horizontal displacements [mm] at minimum twist; (**b**) Corresponding vertical displacements [mm].

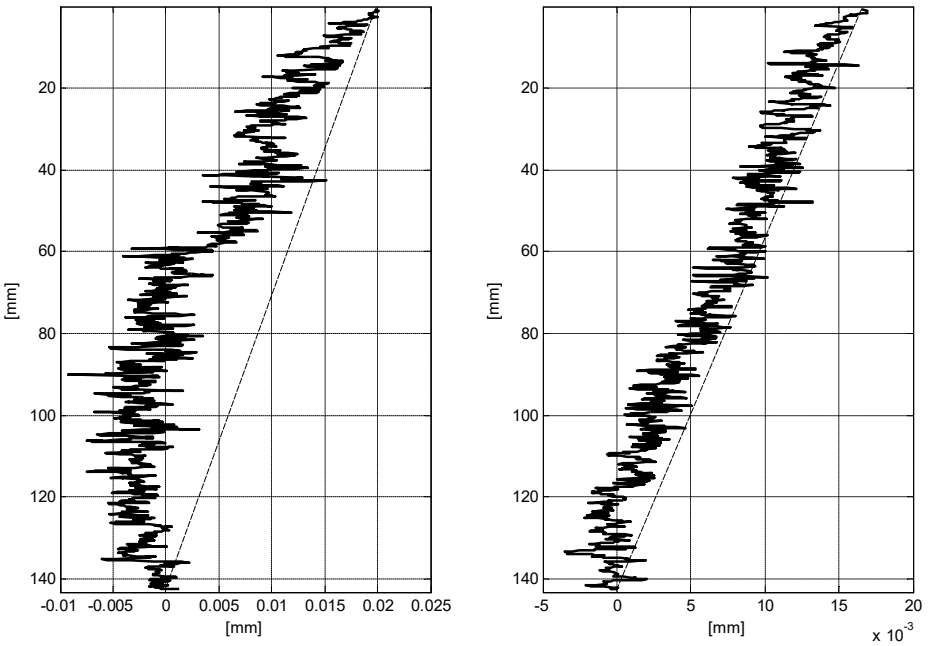

(**a**) (**b**)

Figure 22. Results of optical flow analysis (sample TS1458, averaging width: 10 pixels). (**a**) Horizontal displacements [mm] along the specimen height at minimum twist; (**b**) Corresponding vertical displacements [mm]; (dashed line is the assumed linear relationship between displacement and sample height).

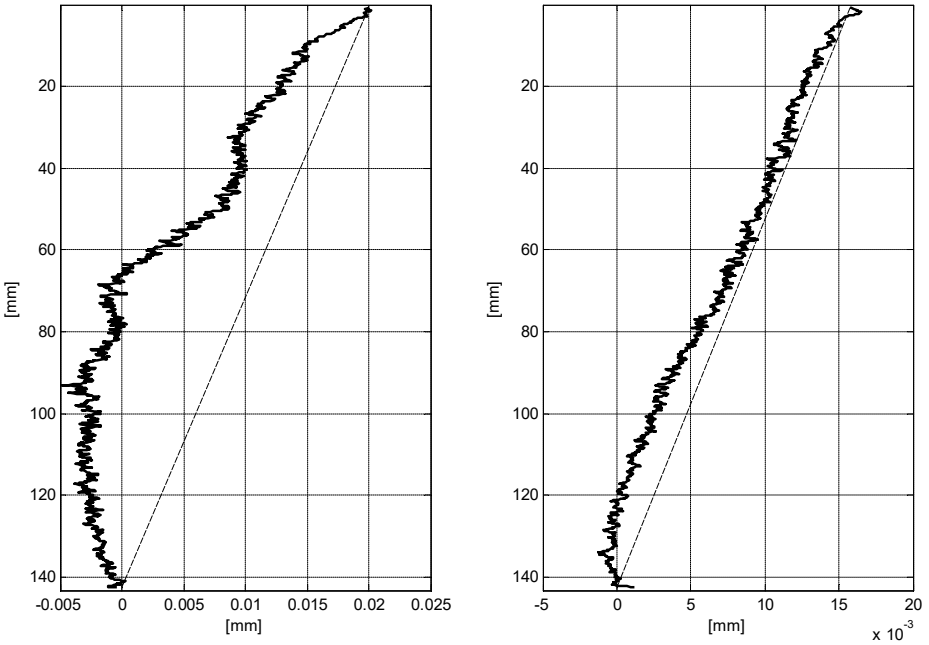

(**a**) (**b**)

Figure 23. Results of optical flow analysis (sample TS1458, averaging width: 200 pixels). (**a**) Horizontal displacements [mm] along the specimen height at minimum twist; (**b**) Corresponding vertical displacements [mm]; (dashed line is the assumed linear relationship between displacement and sample height).

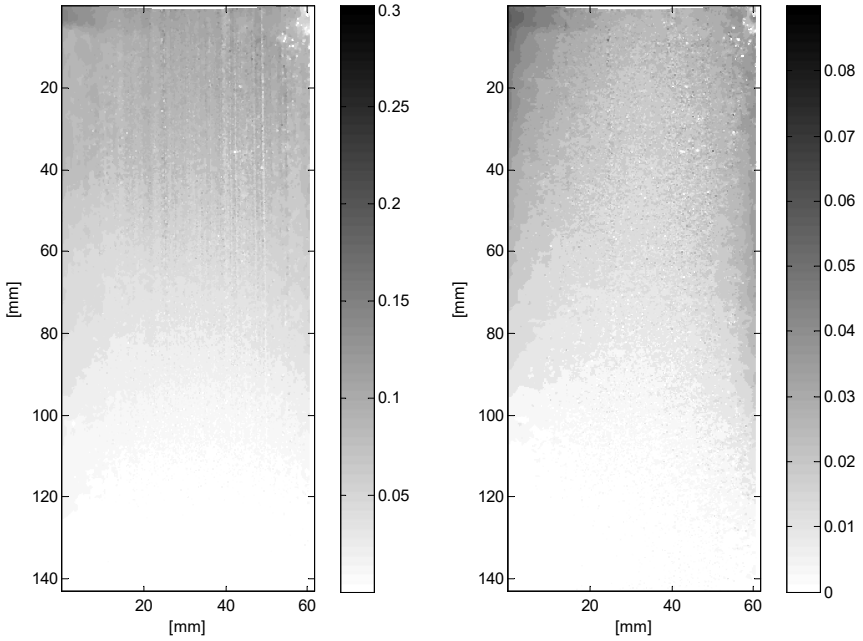

(**a**) (**b**)

Figure 24. Results of optical flow analysis in full resolution (sample TS1458, grid 801x1861 points). (**a**) Residual horizontal displacements [mm]; (**b**) Residual vertical displacements [mm].

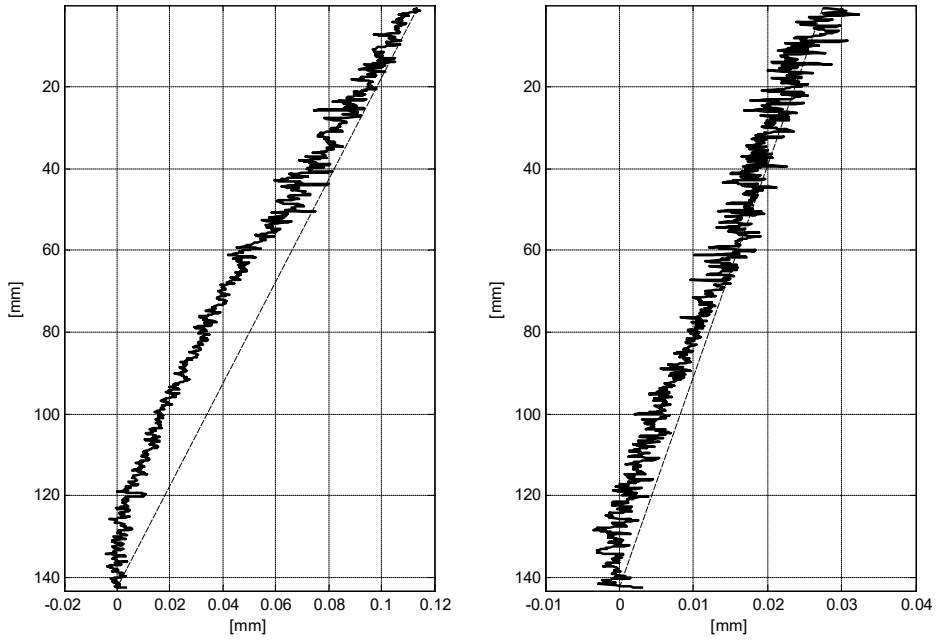

(**a**) (**b**)

Figure 25. Results of optical flow analysis (sample TS1458, averaging width: 10 pixels). (**a**) Residual horizontal displacements [mm]; (**b**) Residual vertical displacements [mm]; (dashed line is the assumed linear relationship between displacement and sample height).

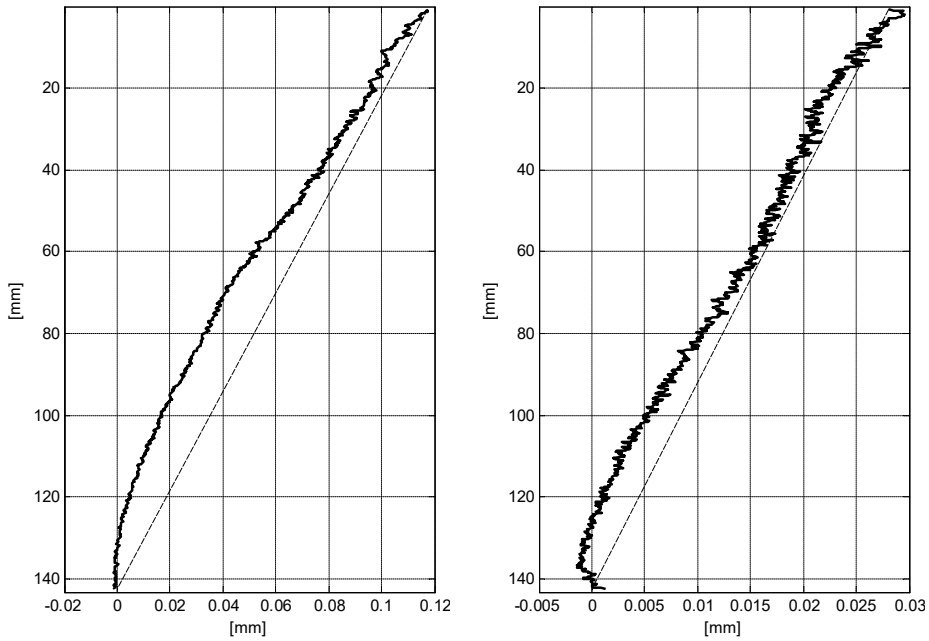

Figure 26. Results of optical flow analysis (sample TS1458, averaging width: 200 pixels). (**a**) Residual horizontal displacements [mm]; (**b**) Residual vertical displacements [mm]; (dashed line is the assumed linear relationship between displacement and sample height).

The results deviate from the assumed linear relationship in terms of shape of the function (clearly non-linear) but they can also lie on either side of that line. An example of this phenomenon can be seen in the results of the TS test carried out on the same sand under a slightly increased isotropic pressure (sample TS5517, see Table 2), which resulted in an increase in the overall rigidity of the sample (see Figure 27).

The results are presented in the same manner as for the first sample. Figures 28-36 show the results for the TS5517 sample. Figures 29-30 show a completely different displacement distribution along the height of the sample (compare to Figures 18-20). It can be stated that the height of the sample responding to the load is variable and depends on many factors, including the internal structure of the tested material, certainly.

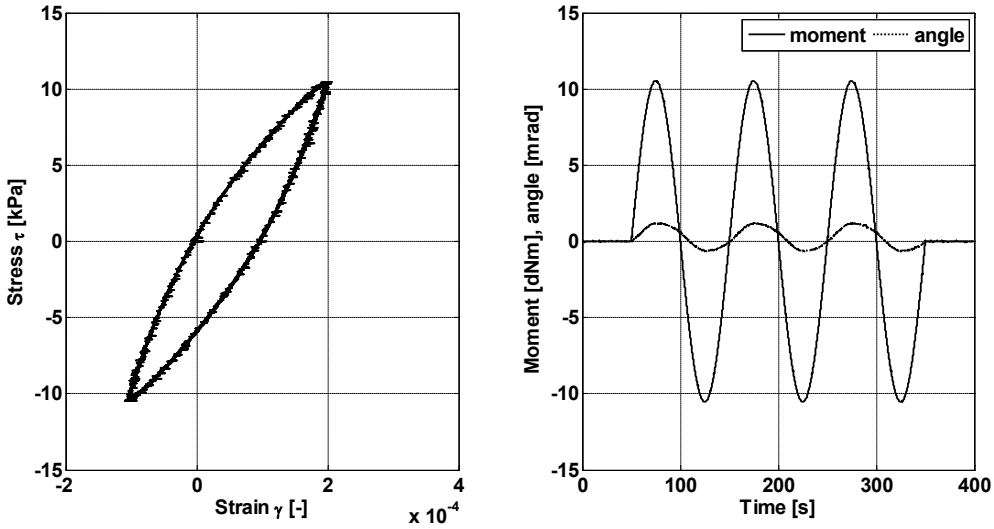

Figure 27. Typical TS test results (sample TS5517)

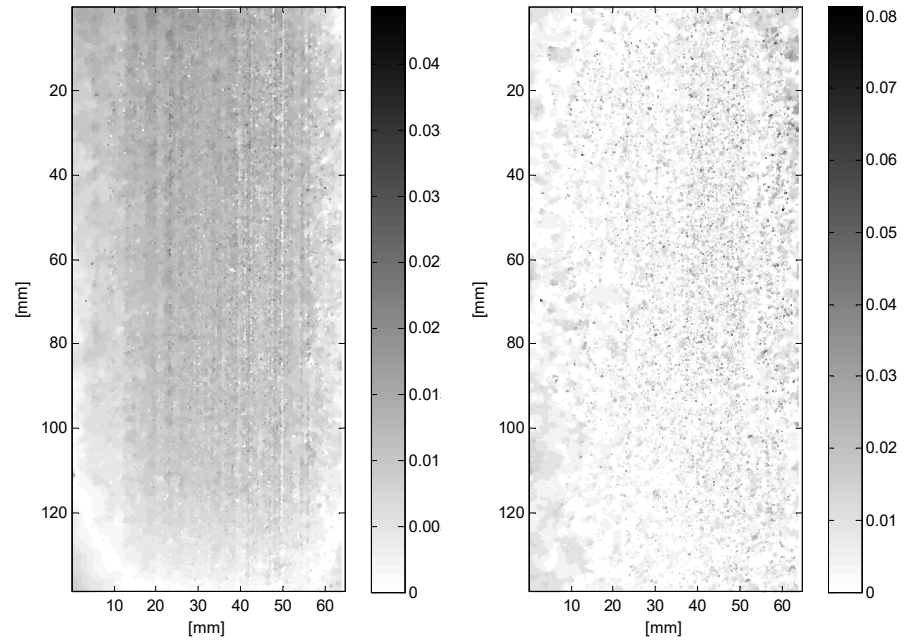

Figure 28. Results of optical flow analysis in full resolution (sample TS5517, grid 801x1861 points). (**a**) Horizontal displacements [mm] along the specimen height at maximum twist; (**b**) Corresponding vertical displacements [mm].

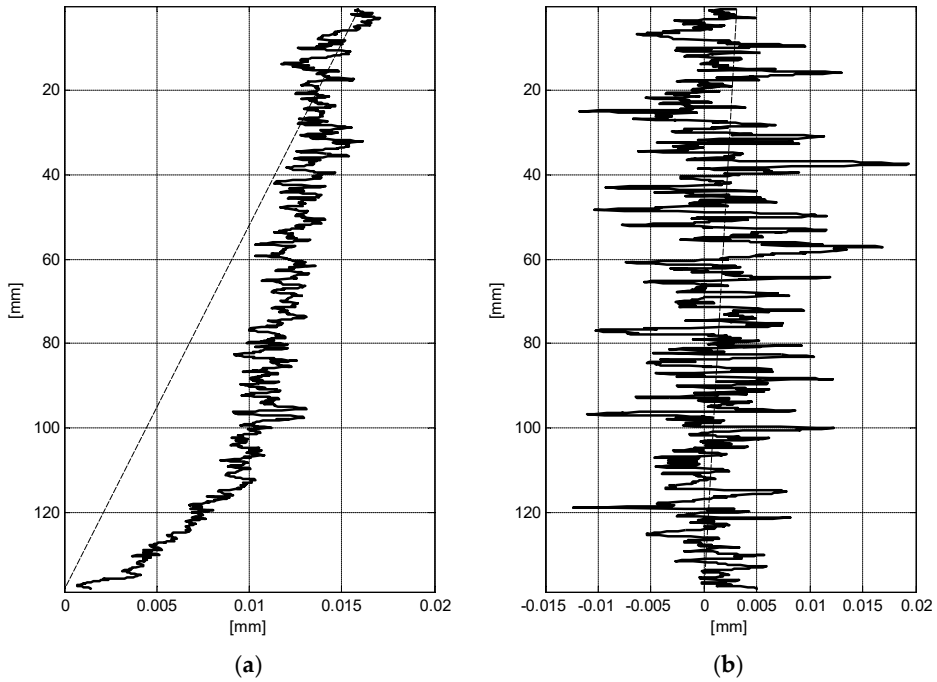

Figure 29. Results of optical flow analysis (sample TS5517, averaging width: 10 pixels). (**a**) Horizontal displacements [mm] along the specimen height at maximum twist; (**b**) Corresponding vertical displacements [mm]; (dashed line is the assumed linear relationship between displacement and sample height).

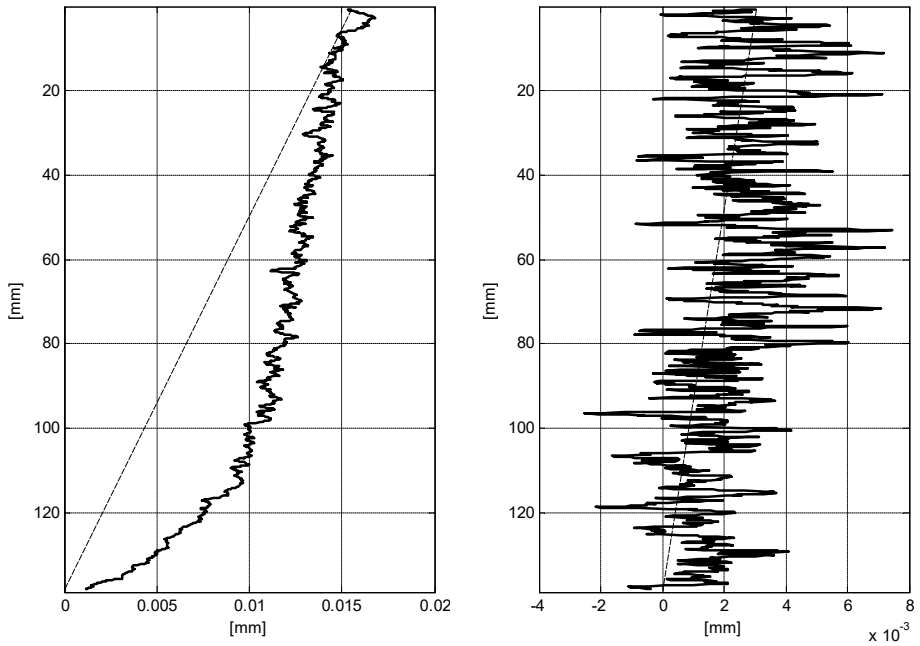

Figure 30. Results of optical flow analysis (sample TS5517, averaging width: 200 pixels). (**a**) Horizontal displacements [mm] along the specimen height at maximum twist; (**b**) Corresponding vertical displacements [mm]; (dashed line is the assumed linear relationship between displacement and sample height).

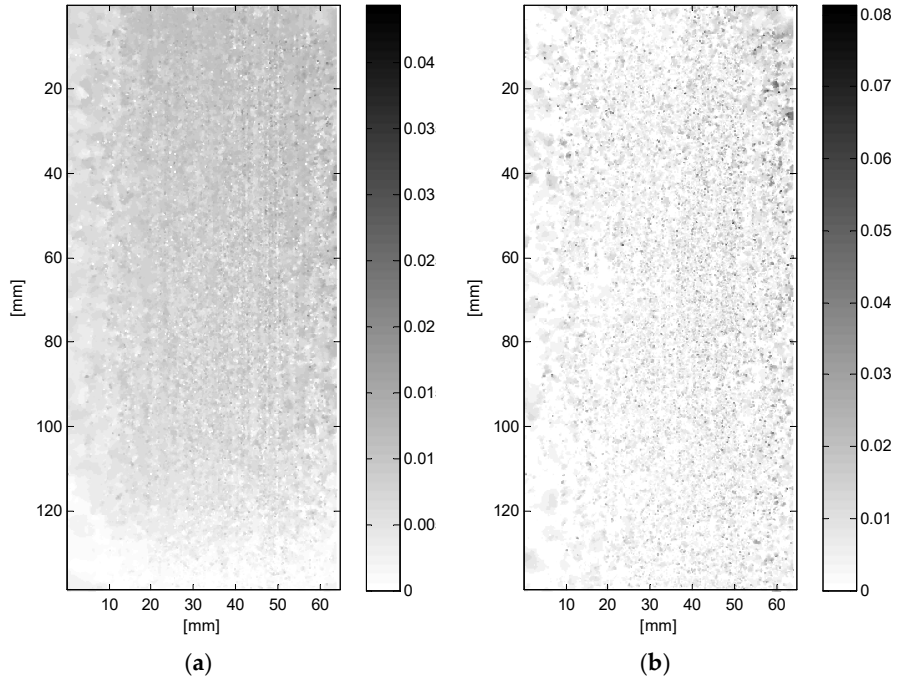

Figure 31. Results of optical flow analysis in full resolution (sample TS5517, grid 801x1861 points). (**a**) Horizontal displacements [mm] at minimum twist; (**b**) Corresponding vertical displacements [mm].

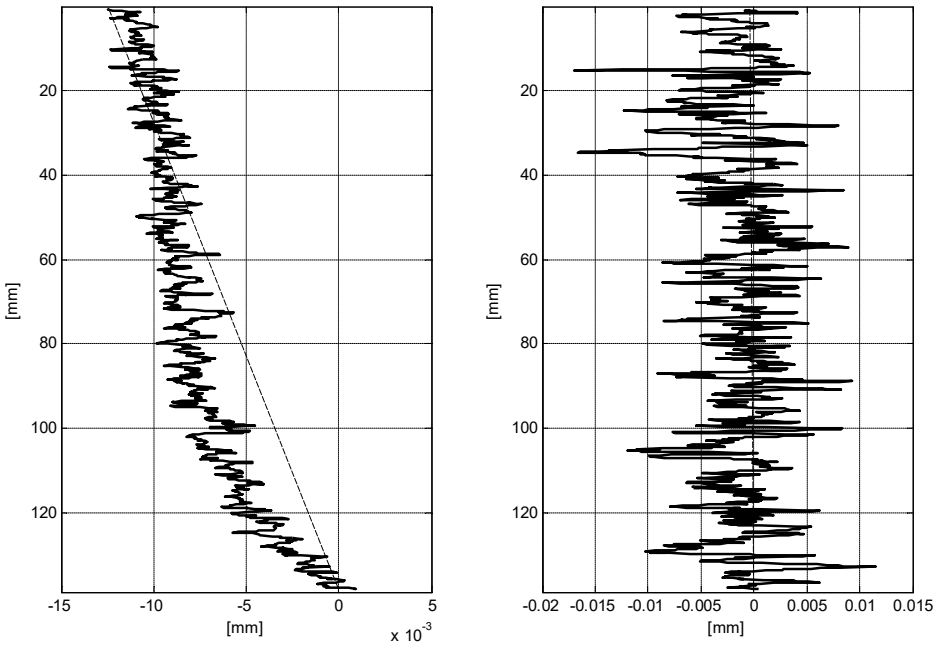

(**a**) (**b**)

Figure 32. Results of optical flow analysis (sample TS5517, averaging width: 10 pixels). (**a**) Horizontal displacements [mm] along the specimen height at minimum twist; (**b**) Corresponding vertical displacements [mm]; (dashed line is the assumed linear relationship between displacement and sample height).

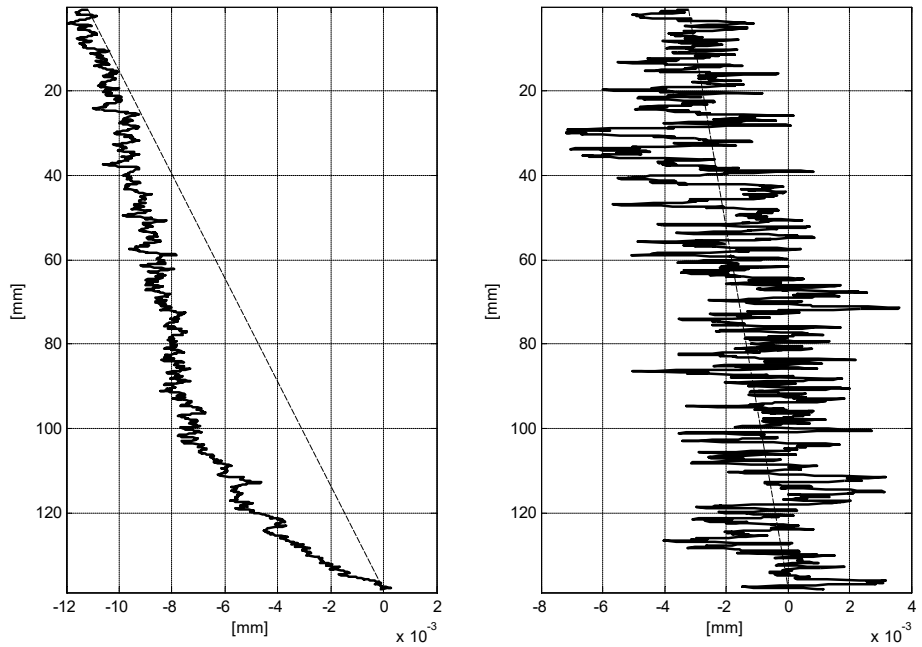

(**a**) (**b**)

Figure 33. Results of optical flow analysis (sample TS5517, averaging width: 200 pixels). (**a**) Horizontal displacements [mm] along the specimen height at minimum twist; (**b**) Corresponding vertical displacements [mm]; (dashed line is the assumed linear relationship between displacement and sample height).

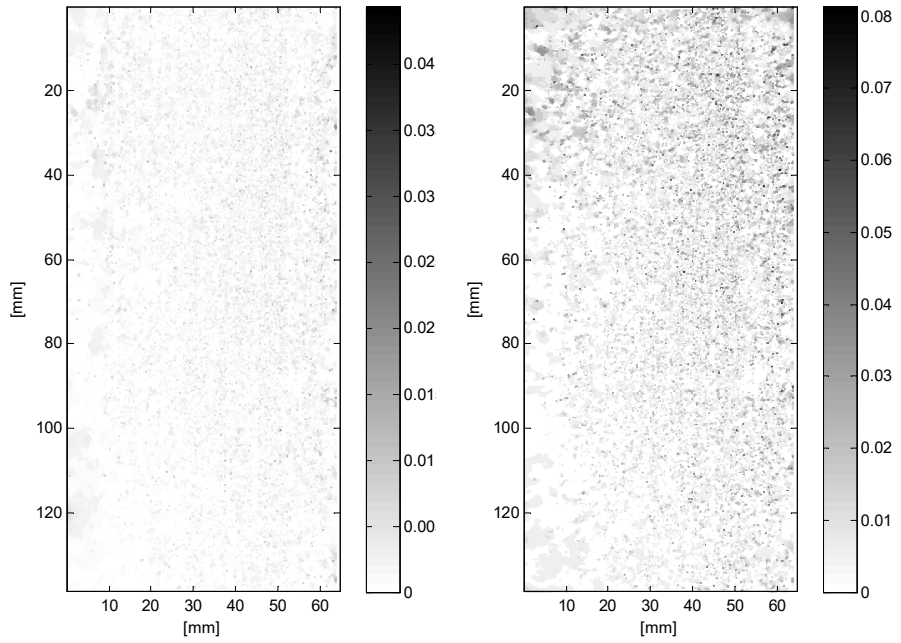

(**a**) (**b**)

Figure 34. Results of optical flow analysis in full resolution (sample TS5517, grid 801x1861 points). (**a**) Residual horizontal displacements [mm]; (**b**) Residual vertical displacements [mm].

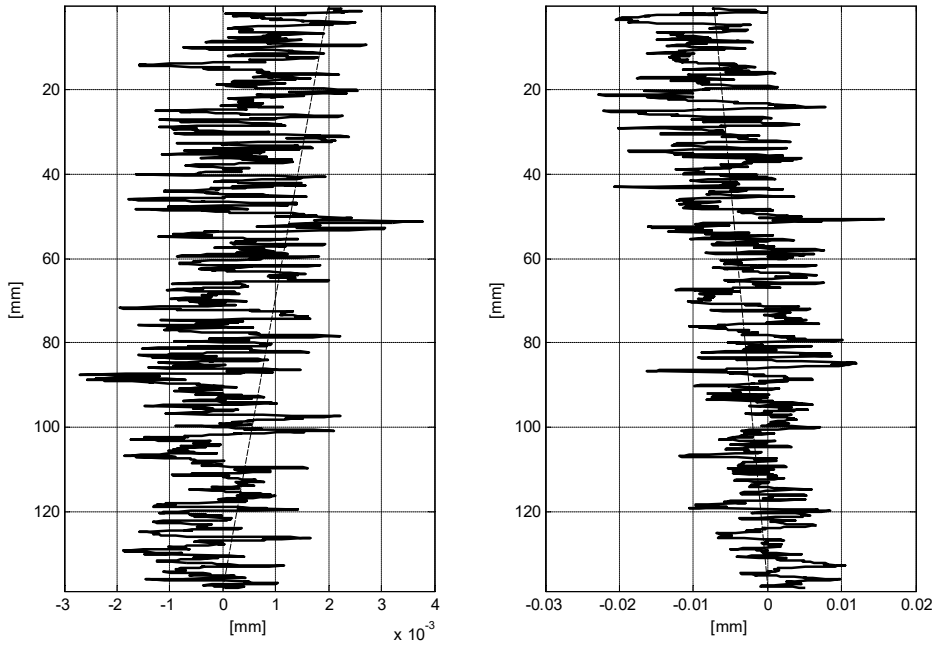

(**a**) (**b**)

Figure 35. Results of optical flow analysis (sample TS5517, averaging width: 10 pixels). (**a**) Residual horizontal displacements [mm]; (**b**) Residual vertical displacements [mm]; (dashed line is the assumed linear relationship between displacement and sample height).

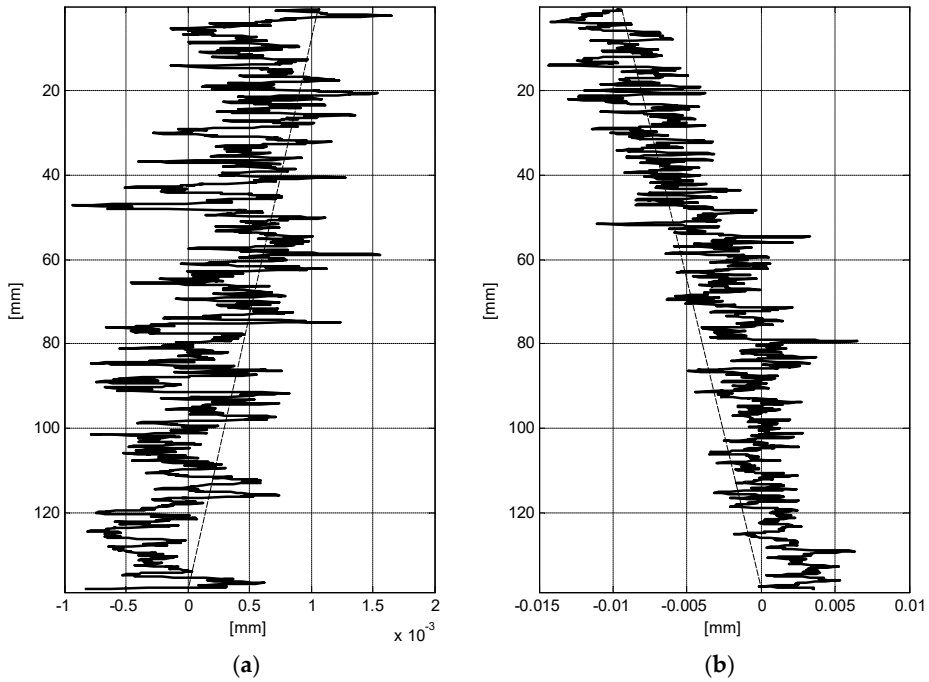

Figure 36. Results of optical flow analysis (sample TS5517, averaging width: 200 pixels). (**a**) Residual horizontal displacements [mm]; (**b**) Residual vertical displacements [mm]; (dashed line is the assumed linear relationship between displacement and sample height).

4. Discussion

A direct result of the performed analyzes is a proposed preliminary simplified mechanism of deformation of non-cohesive soil samples during torsion, presented in Figure 37. This simplification is based on an assumption that the deformation mechanism is bi-linear. In the first case, the modification of assumed deformation distribution is taking into account the shortened height of the sample h' (Figure 37(a)). The second case (Figure 37(b)) is more difficult to describe due to the strongly non-linear soil stiffness degradation in the range of observed strains. This problem was taken up in further research, the scope of which goes beyond the scope of this work.

It is obvious that the optical flow method is sensitive to pixel dimensions in analyzed images. This is well visible in Figures 26 and 36 where the observed displacement to the pixel dimension ratio is large and small, respectively. It should also be noted that the resolution of the results obtained is greater than the dimension of a single pixel in registered images (approx. 0.07 mm), which results from the complex analysis of separated pixel systems and consideration of changes in their brightness. This undoubted advantage can, however, cause a lot of trouble in practice. An example is the result shown in Figure 38. While recording this particular photo, someone entered the laboratory and their reflection in the external cylinder of the testing device chamber can be seen. The result is visible as a cloud of darker points in the center of the image. Additionally, small uncontrolled movement of objects near the system leads to false results. Another problem is the quality of the transparent cylinders covering the RC/TS device. Material flaws invisible to the naked eye are revealed in the results of the analyzes. For example, traces resulting from tailored forming of the inner cylinder can be seen in Figures 17(a) and 28(a) in the form of vertical light and dark lines. Of course, this kind of distortion can be eliminated in the results by using appropriate filters (or eventually manual correction). On the other hand, this sensitivity of the method can be successfully used to identify flaws and imperfections in transparent and reflective materials.

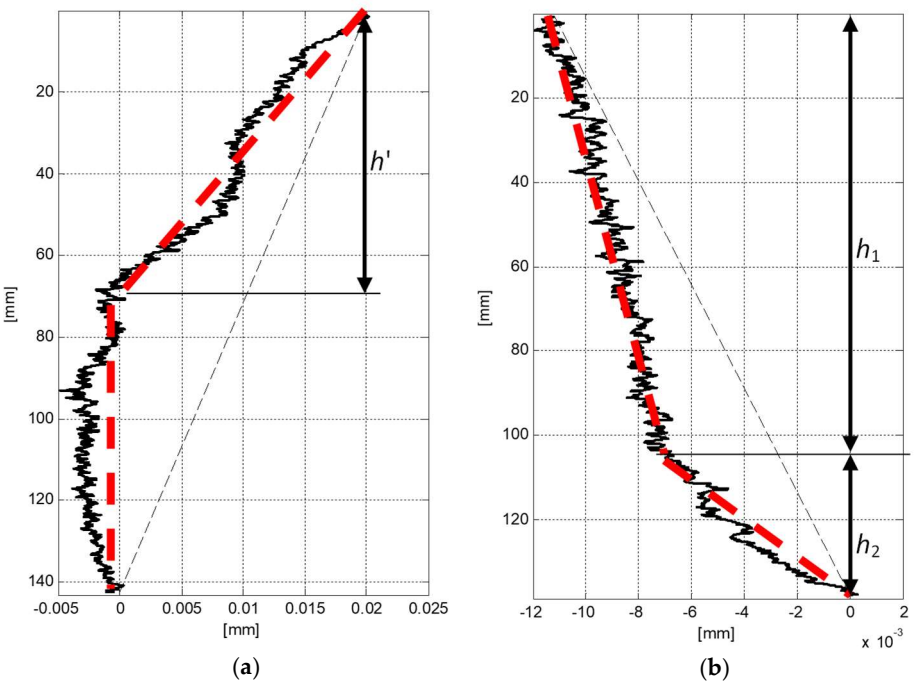

(**a**) (**b**)

Figure 37. Results of optical flow analysis. Simplified deformation mechanism (averaging width: 200 pixels). (**a**) TS1458; (**b**) TS5517; (dashed line is the assumed linear relationship between displacement and sample height bold red dashed line is the simplified form of horizontal displacement).

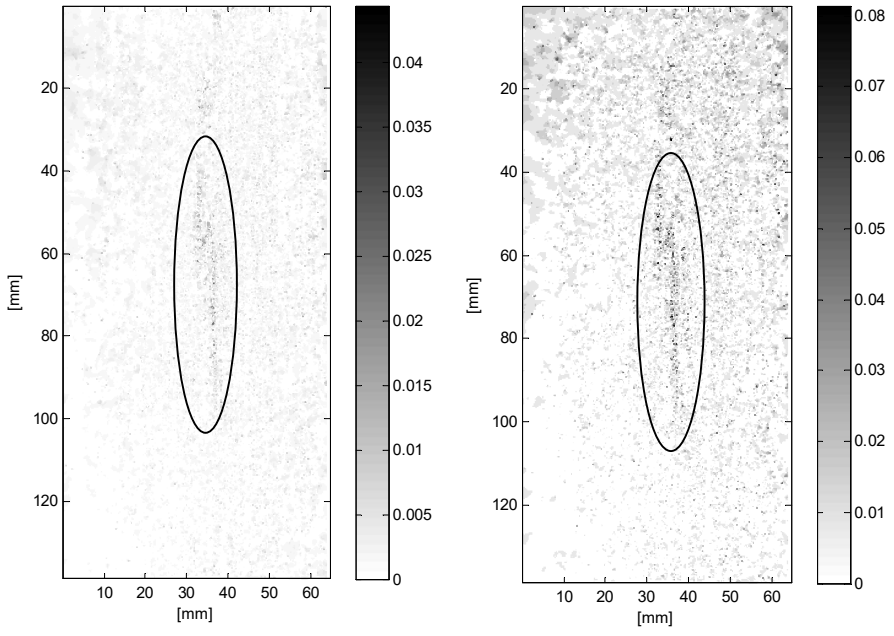

(**a**) (**b**)

Figure 38. Results of optical flow analysis in full resolution (sample TS5517, grid 801x1861 points). (**a**) Residual horizontal displacements [mm]; (**b**) residual vertical displacements [mm].

5. Conclusions

The obtained results justify the conclusion that while the displacement values change approximately monotonically along the sample height, the shape of displacement function is very different for samples under different isotropic pressure. Moreover, the deviations from the assumed linearity distribute differently on sample's height during different stages of the same TS test.

It cannot be unequivocally determined how much of the sample height undergoes systematic deformation during TS tests, and therefore authors suggest that measurements of displacements on the side surface of the sample should always accompany such tests. The correctly determined "active" height of the sample is one of the most important conditions for the correct estimation of the soil stiffness modulus in laboratory tests. The results presented in this paper signal the possibility that the deformation calculated from the rotation angle measured using proximity sensors can be seriously underestimated. As the angle measurements are used for determining the nonlinear stiffness degradation characteristics, e.g. $G(\gamma)$ functions, the error is propagated to the geomechanical modelling and the structural design process.

The authors will continue their work on observing non-linear soil deformations (in small strain range) and taking those observations into account in the torsional shearing tests results interpretation.

The optical flow techniques are being intensively developed but the progress in measurement of small deformations in soils is constantly insufficient. Therefore, the research team intends to continue searching for optimal measurement conditions and image recording techniques so that the quality of the results obtained from optical flow method is as high as possible and ready to use in engineering practice.

Author Contributions: Conceptualization, P.S. and M.B.(1); methodology, P.S.; software, P.S.; validation, P.S., M.B.(1), M.B.(2) and R.O.; formal analysis, M.B.(2) and R.O.; investigation, M.B.(1); writing—original draft preparation, P.S. and M.B.(2); writing—review and editing, M.B.(2); visualization, M.B.(1); supervision, P.S., M.B.(2) and R.O. All authors have read and agreed to the published version of the manuscript.

Funding: This research received no external funding.

Conflicts of Interest: The authors declare no conflict of interest.

References

1. Ce, L., Beyond pixels: exploring new representations and applications for motion analysis. PhD Thesis, Massachusetts Institute of Technology, USA, 2009.
2. Terzaghi, K., Erdbaumechanik auf bodenphysikalischer grundlage. Leipzig u. Wien, F. Deuticke, 1925.
3. Chen, W.-F., Liu, X.L., Limit analysis in soil mechanics. *Developments in geotechnical engineering*, vol. 52, Elsevier, 1990.
4. Look, B.G., Handbook of geotechnical investigation and design tables. Taylor & Francis, 2007.
5. Chen, W.-F., Limit analysis and soil plasticity. *Developments in geotechnical engineering*, vol. 7, Elsevier, 1975.
6. Lade, P.V., Elasto-plastic stress-strain theory for cohesionless soil with curved yield surfaces. *International Journal of Solids and Structures,* 13(11), 1977, 1019-1035.
7. Chen, W.-F., Constitutive equations for Engineering Materials. Plasticity and modeling. *Studies in Applied Mechanics*, vol. 37. Elsevier, 1994.
8. Potts, D.M., Zdravkovič, L., Finite element analysis in geotechnical engineering. Theory. Thomas Telford, 1999.
9. Puzrin, A.M., Constitutive modelling in geomechanics: introduction. Springer, 2012.
10. Jardine, R.J., Potts, D.M., Fourie, A.B., Burland, J.B., Studies of the influence of non-linear stress-strain characteristics in soil-structure interaction, *Gotechnique,* 36(3), 1986, 377-396.
11. Fares, R., Santisi, d'Avila, M.P., Deschamps, A., Soil-structure interaction analysis using a 1DT-3C wave propagation model. *Soil Dynamics and Earthquake Engineering*, 2019, 120, 200-213.
12. Jardine, R.J., Potts, D.M., Fourie, A.B., Burland, J.B., Studies of the influence of nonlinear stress-strain characteristics in soil-structure interaction. *Geotechnique*, 1986, 36(3), 377-396.
13. Puzrin, A.M., Burland, J.B., Non-linear model of small-strain behaviour of soils. *Geotechnique*, 48(2), 1998, 217-233.
14. Benz, T., Small strain stiffness of soils and its numerical consequences. PhD thesis, University of Stuttgart, 2007.
15. Cudny, M., Truty, A., Refinement of the Hardening Soil model within the small strain range. Acta geotechnica, 15, 2020, 2031–2051.

16. Muir Wood, D., Modelling and testing. 19th International Conference on Soil Mechanics and Geotechnical Engineering, Honours Lectures, 2017.
17. Desrues, J., Viggiani, G., Bésuelle, P., (Eds.), Advances in X-ray tomography for geomaterials. ISTE, 2006.
18. Tyrologou, P., Dudeney, A.W.L., Grattoni, C.A., Evolution of porosity in geotechnical composites. *Magnetic Resonance Imaging*, 23(6), 2005, 765-768.
19. Kong, L., Sayem, H.M., Tian, H., Influence of drying–wetting cycles on soil-water characteristic curve of undisturbed granite residual soils and microstructure mechanism by nuclear magnetic resonance (NMR) spin-spin relaxation time (T2) relaxometry. *Canadian Geotechnical Journal,* 55(2), 2018, 208-216.
20. Iskander, M., Optical Techniques in Geotechnical Engineering. *Modelling with Transparent Soils*. Springer Series in Geomechanics and Geoengineering. Springer, 2010.
21. Gill, D., Lehane, B., An optical technique for investigating soil displacement patterns. *Geotechnical Testing Journal*, 2001, 24(3), 324-329, DOI: 10.1520/GTJ11351J.
22. Kuang, K.S.C., Wireless chemiluminescence-based sensor for soil deformation detection. *Sensors and Actuators*, 2018, 269, 70–78.
23. Xu, D.-S., A new measurement approach for small deformations of soil specimens using fiber bragg grating sensors. *Sensors*, 2017, 17(5), 1016, DOI:10.3390/s17051016.
24. White, D.J., Take, W.A., Bolton, M.D., Soil deformation measurement using particle image velocimetry (PIV) and photogrammetry. *Geotechnique*, 2003, 53(7), 619–631.
25. Horn, B.K.P., Schunck, B.G., Determining optical flow. *Artificial Intelligence*, 1981, 17(1–3), 185-203, DOI:10.1016/0004-3702(81)90024-2
26. Gibson, J.J., The perception of the visual world". *Houghton Mifflin Company*, Boston, 1950.
27. Kelson, R.T.A., Santana, A.M., Medeiros, A.A.D., Optical flow using color information. Proceedings of the 2008 ACM Symposium on Applied Computing (SAC), Fortaleza, Ceara, Brazil, 16-20 March 2008, DOI: 10.1145/1363686.1364064.
28. Gultekin, G. K., Saranli, A., An FPGA based high performance optical flow hardware design for computer vision applications. *Microprocessors and Microsystems,* 2013, vol. 37(3), 270-286.
29. Chauhan V., Surgenor, B., Fault detection and classification in automated assembly machines using machine vision. *The International Journal of Advanced Manufacturing Technology*, 2017, vol. 90, 2491–2512.
30. Rateke, T., von Wangenheim, A., Road obstacles positional and dynamic features extraction combining object detection, stereo disparity maps and optical flow data. *Machine Vision and Applications*, 2020, vol. 31, article number: 73.
31. Barrows, G. L., Chahl, J. S. and Srinivasan, M. V., Biologically inspired visual sensing and flight Control. *Aeronautical Journal*, 2003, 107 (1069), 159–268.
32. Dong, C.-Z., Celik, O., Necati Catbas, F., O'Brien, E.J., & Taylor, S., Structural displacement monitoring using deep learning-based full field optical flow methods, *Structure and Infrastructure Engineering*, 2020, 16:1, 51-71.
33. Hartmann, C., Wang, J., Opristescu, D., Volk, W., Implementation and evaluation of optical flow methods for two-dimensional deformation measurement in comparison to digital image correlation. *Optics and Lasers in Engineering*, 2018, 107, 127-141.
34. González-Acuña, R.G., Dávila, A., Gutiérrez-Vega, J.C., Optical flow of non-integer order in particle image velocimetry techniques. *Signal Processing*, 2019, 155, 317–322.
35. Tu, Z., Xie, W., Zhang, D., Poppe, R., Veltkamp, R.C., Li, B., Yuan, J., A survey of variational and CNN-based optical flow techniques. *Signal Processing: Image Communication*, 2019, 72, 9–24.
36. Ishimoto, M., Iida, K., Determination of elastic constants by means of vibration methods, part 1, Young's modulus. *Bulletin of Earthquake Research Institute*, 1936; 14, 632–657.
37. Birch, F., Bancroft, D., Elasticity and internal friction in a long column of granite. *Bulletin of the Seismological Society of America*, 1938, 28, 243-254.
38. Kim, D.S., Stokoe, K.H., Deformational characteristics of soils at small to medium strains. *Earthquake Geotechnical Engineering*, 1995; Tokyo, Japan, 89-94.
39. Madhusudhan, B.N., Senetakis, K., Evaluating use of resonant column in flexural mode for dynamic characterization of Bangalore sand. *Soils and Foundations*, 2016, 56(3), 574-580.
40. Senetakis, K., Payan, M., Small strain damping ratio of sands and silty sands subjected to flexural and torsional resonant column excitation. *Soil Dynamics and Earthquake Engineering*, 2018, 114, 448-459.

41. Senetakis, K., Anastasiadis, A., Pitilakis, K., A comparison of material damping measurements in resonant column using the steady-state and free-vibration decay methods. *Soil Dynamics and Earthquake Engineering*, 2015, 74, 10-13.
42. Khan, Z., El Naggar, M.H., Cascante, G., Frequency dependent dynamic properties from resonant column and cyclic triaxial tests. *Journal of the Franklin Institute*, 2011, 348(7), 1363-1376.
43. Hoyos, L.R., Suescún-Florez, E.A., Puppala, A.J., Stiffness of intermediate unsaturated soil from simultaneous suction-controlled resonant column and bender element testing. *Engineering Geology*, 2015, 188, 10-28.
44. Chong, S.-H., Kim, J.-Y., Nonlinear vibration analysis of the resonant column test of granular materials, *Journal of Sound and Vibration*, 2017, 393, 216-228.
45. Cabalar, A.F., Applications of the oedometer, triaxial and resonant column tests to the study of micaceous sands. *Engineering Geology*, 2010, 112(1–4), 21-28.
46. Bae, Y.-S., Bay, J.A., Modifications of resonant column and torsional shear device for the large strain. *Computers and Geotechnics*, 2009, 36(6), 944-952.
47. Bujko, M., Identification of elasto-plastic phenomena in soils in the range of small strains. World Multidisciplinary Civil Engineering-Architecture-Urban Planning Symposium, 18-22 June 2018, IOP Conference Series Materials Science and Engineering, 2018, 471, 042013, DOI: 10.1088/1757-899X/471/4/042013.
48. Srokosz, P.E., Dyka, I., Bujko, M., Interpretation of shear modulus degradation tests. *Studia Geotechnica et Mechanica*, 2018, 40(2), 125-132.
49. Dyka, I., Srokosz, P.E., Soil testing in the RC/TS apparatus. Part 1. *Inżynieria Morska i Geotechnika*, 2012, 6, 700-707 (available in english: http://www.controls-group.com/DownLoadFileUrl.php/url=backend@@download@@file_upload@@file@@140514101960_soil_testing_in_the_rc_ts_apparatus._part_1_e.pdf/nomefile=soil_testing_in_the_rc_ts_apparatus._part_1_e.pdf).
50. Bujko, M., Srokosz, P.E., Dyka, I., Use of optical method for improvement of soil dynamic tests in torsional shear apparatus. Baltic Geodetic Congress (BGC Geomatics), 22-25 June 2017, Gdansk, Poland, 404-408.
51. Dyka, I., Srokosz, P.E., Bujko, M., Influence of grain size distribution on dynamic shear modulus of sands. *Open Engineering*, 2017, 7(1), 317-329.
52. Fleet, D.J., Weiss, Y., Optical flow estimation. *Handbook of Mathematical Models in Computer Vision*, 2006; DOI:10.1007/0-387-28831-7_15.
53. Andrews, R.J., Lovell, B.C., Color Optical Flow. Proceedings of the 2003 APRS Workshop on Digital Image Computing, Brisbane, Publisher: Australian Pattern Recognition Society, 2003.
54. Lucas, B., Kanade, T., An iterative image restoration technique with an application to stereo vision. Proceedings of the DARPA IU Workshop, 1981, 121-130.
55. Barron, J.L., Fleet, D.J., Beauchemin, S.S., Performance of optical flow techniques. *International Journal of Computer Vision*, 1994; 12(1), 43-77, DOI: 10.1007/BF01420984.
56. Ohta, N., Optical flow detection by color images. Proceedings of IEEE International Conference on Image Processing, 1989, 801-805.
57. Golland, P., Bruckstein, A.M., Motion from color. Technical report, Computer Science Department, Technion, IIT, 1997, Haifa, Israel.
58. Lowe, D.G., Object recognition from local scale-invariant features. Proceedings of IEEE International Conference on Computer Vision (ICCV), 1999, Kerkyra, Greece, 1150–1157.
59. Erdogan, K., Yilmaz, N., Shifting colors to overcome not realizing objects problem due to color vision deficiency. Proceedings of the 2nd International Conference on Advances in Computing, Electronics and Electrical Technology – CEET, 2014, Kuala Lumpur, Malaysia, 11-14.
60. De Greve, B., Reflections and refractions in ray tracing. Available online: https://graphics.stanford.edu/courses/cs148-10-summer/docs/2006--degreve--reflection_refraction.pdf (accessed on 27 July 2020).
61. Ciddor, P.E., Refractive index of air: new equations for the visible and near infrared. *Appl. Optics*, 1996, 35, 1566-1573.
62. Sultanova, N., Kasarova, S., Nikolov, I., Dispersion properties of optical polymers. *Acta Physica Polonica A*, 2009, 116, 585-587.